

Redesigning the Post Amplifier Module for the Allen Telescope Array Radio Telescope

Monika Schäfer

University of Applied Science Munich

practical semester report

April 01, 2025

Abstract

This report presents the design, optimization, and evaluation of different prototypes for the Post Amplifier Module (PAM), a crucial component for controlling RF signal gain in radio astronomy antennas. The goal is to replace the 20-year-old PAM of the Allen Telescope Array (ATA) to enhance its sensitivity and extend the bandwidth to 1–20 GHz. The optimization process includes refining the signal trace design to reduce losses and improve impedance matching. Furthermore, two amplifier options are tested and the most suitable one is chosen for the design. In addition, a design that integrates multiple amplifiers and attenuators into the existing PAM enclosure is investigated. Finally, a modular design approach in which the PAM components are distributed across several smaller enclosures is presented as the preferred solution.

Contents

1	Introduction	5
1.1	Allen Telescope Array	5
1.2	Post Amplifier Module	5
1.3	Initial Project Status and Design Framework	7
2	Optimization of the Signal Trace	8
2.1	Coplanar Waveguide	8
2.2	S-Parameters	9
2.3	Evaluation of a Previous Prototype and Trace Modeling	10
2.4	Optimization of the Signal Trace for the First Prototype	13
2.5	Prototype and Experimental Results	15
2.6	Summary	16
3	Selection of an Appropriate Amplifier	17
3.1	Design of the HMC462-Based Prototype	17
3.2	Design of the MML098GQ4A-Based Prototype	19
3.3	Assembly and Measurement of the HMC462-Based Prototype	21
3.4	Assembly and Measurement of the MML098GQ4A-Based Prototype	24
3.5	Summary	26
4	Cascading Amplifiers and Attenuators	27
4.1	Design	27
4.2	Measurement	30
4.3	Summary	34
5	A Modular Design Approach	35
5.1	Overview of different Modules	35
5.2	Simulations and Optimizations	36
5.3	Amplifier Module	39
5.4	Attenuator Module	41
5.5	Detector Module	45

5.6	Summary	50
6	Conclusion	51
References		52

1 Introduction

1.1 Allen Telescope Array

The Allen Telescope Array (ATA) is a radio astronomy telescope located in Hat Creek, California. It was dedicated in 2007 as a collaborative effort between the SETI Institute and the University of California in Berkeley, with funding support from Microsoft co-founder Paul Allen. [1] Designed primarily for the Search for Extraterrestrial Intelligence (SETI), the ATA also plays a significant role in a variety of scientific investigations, including the study of fast radio bursts (FRBs), slow transients, and pulsars. The ATA operates within a frequency range from 1 to 10 GHz. [2]

The array consists of 42 individual antennas, each with a diameter of approximately six meters, operating together as an interferometric array. Currently, 20 of these antennas are actively used for observations, while an ongoing refurbishment program aims to restore the entire array to full functionality. This effort will significantly enhance its sensitivity. [2]

1.2 Post Amplifier Module

The Post Amplifier Module (PAM) is located inside of the ATA antennas, after the feed horn. It contains several amplifiers, as well as variable attenuators to control the gain of the incoming radio signal. Figure 1 shows the PAM that is inside of the antennas since their dedication in 2007.

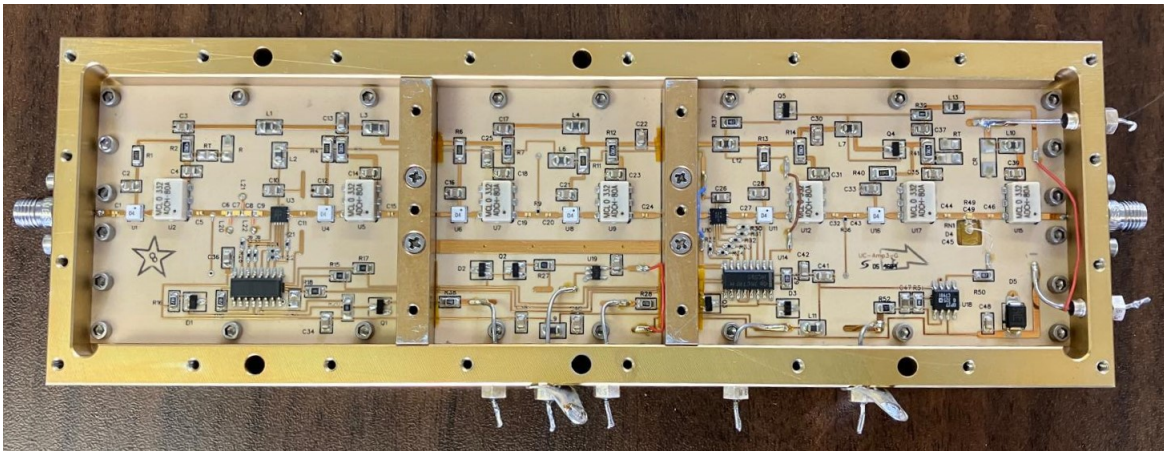


Figure 1: ATA PAM from 2007.

The PAMs signal path, running between the two SMA connectors, includes five amplifiers, each providing 12 dB of gain, and two 6-bit attenuators, capable of adjusting the mitigation from 0 to -31.5 dB. The components positioned above the signal line ensure a stable power supply to the amplifiers, while most of the components below the signal line are dedicated to controlling the attenuators. [3]

One key parameter in evaluating the effectiveness of the PAM is the insertion loss. It characterizes how much signal power is lost as it passes through the module and will be explained further in Section 2.2. Figure 2 presents the measured insertion loss of the original PAM from 2007 in decibels.



Figure 2: Insertion Loss of the ATA PAM from 2007. The figure was taken from the GitHub page of the Hat Creek Radio Observatory (HCRO) [3].

For this measurement, the attenuators were set to achieve an output gain of approximately 30 dB. While the insertion loss remains fairly close to that value between 0.5-10 GHz, it shows a significant drop off outside this range.

Currently, only 20 of the 42 antennas are equipped with PAMs, with only two spare modules available. This is enough for one additional antenna, as one PAM is needed per polarization. Furthermore, several components used in the 2007 PAM design are now

obsolete, posing challenges for maintenance and expansion. To fully restore the array and improve its performance, a redesigned PAM is required, which is the subject of this report.

1.3 Initial Project Status and Design Framework

At the start of this project, a preliminary schematic for the new PAM had already been developed by a previous contributor. It is shown in Figure 3.

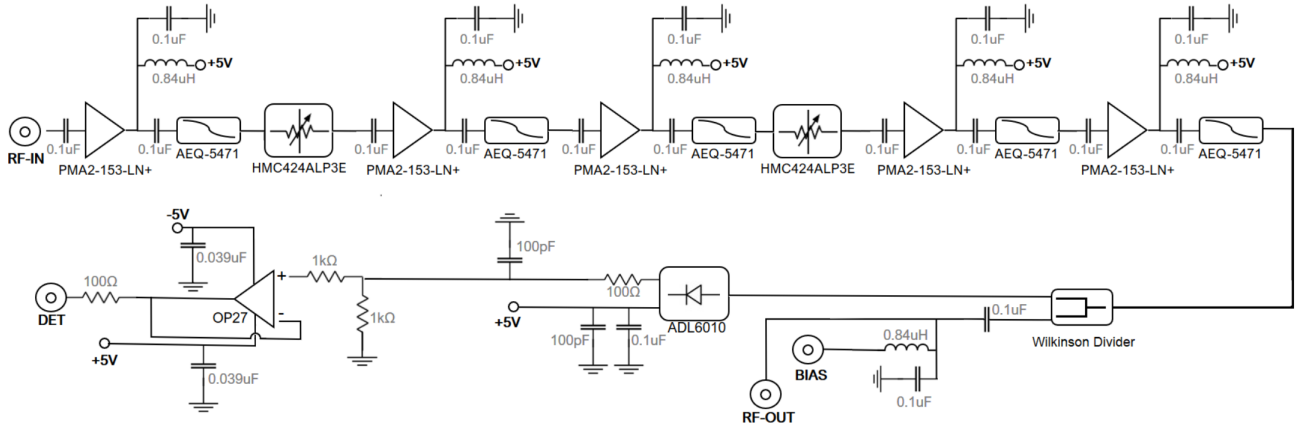


Figure 3: Schematic for the new PAM module at the beginning of project. It was taken from the GitHub page of the HCRO [3].

In the upper half of the schematic, amplifiers, gain equalizers, and variable attenuators are arranged in a repeating sequence. Gain equalizers compensate for the negative gain slope introduced by amplifiers or transmission lines. To ensure a stable +5 V supply for the amplifiers, bias tees are used. These circuit components inject DC power into the signal path while preventing interference between the RF signal and the power supply.

In the lower section of the schematic, a Wilkinson divider splits the signal into two paths. One path leads to a detector diode, which measures the signal power — an essential step for properly adjusting the variable attenuators in the upper section. The second path serves as the RF output. Additionally, a separate output extracts the DC component of the RF signal, which is required for coax-to-fiber conversion after the PAM. This conversion enables a low-loss transfer of the signal from the antenna to the signal processing room.

With the schematic already defined, the next step was to consider the design requirements that guided the development of the new PAM. The target bandwidth for the new PAM extends from 1 to 20 GHz, with an insertion loss of less than -10 dB. To ensure compatibility with other antenna components, the impedance must be 50 ohms. In addition, fitting the new PAM into the existing enclosure would be beneficial, as it would save fabrication costs for new enclosures.

Due to the complexity of high-frequency designs, a step-by-step prototyping approach was taken. The first prototype included only the signal trace, with components gradually introduced in later iterations. This method helped isolate potential issues, making troubleshooting more efficient. To optimize trace layouts and component connections, the High Frequency Structure Simulator (HFSS) from Ansys was used. PCB designs were created in Altium Designer, and to minimize costs, all components were soldered by hand.

2 Optimization of the Signal Trace

This chapter describes the first prototype of the PAM, which consists solely of the signal trace without any components. It begins with a brief introduction to coplanar waveguides and S-parameters, followed by a description of the simulation and optimization process for the signal trace. Finally, the measurements of the manufactured prototype are presented.

2.1 Coplanar Waveguide

A coplanar waveguide (CPW) is often used in high-frequency circuit designs to design a low-loss signal trace. Figure 4 illustrates the structure of a CPW.

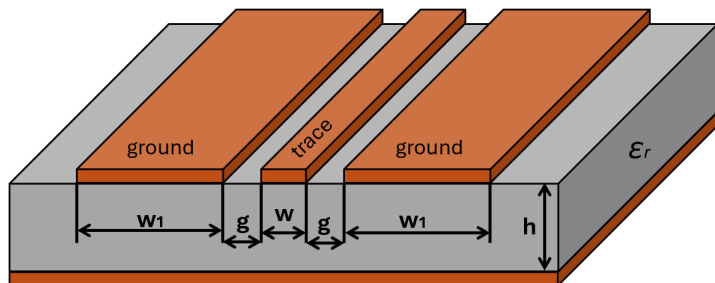


Figure 4: structure of a coplanar waveguide (CPW).

On top of the substrate (gray), the signal trace runs between two grounded metal planes. If the substrate and ground planes are sufficiently large ($h \geq 3w$, $h \geq 3g$ and $w_1 \geq 3w$), the electrical characteristics depend primarily on the trace width w and the gap width g and not on the substrate thickness h . This is beneficial because the substrate thickness can vary by 1% - 5% due to manufacturing tolerances, leading to a similar variation in impedance. To ensure compatibility of the PAM with other antenna components, it is crucial to match the impedance of 50 ohms as closely as possible. Lateral dimensions such as w and g are more precisely controlled by photolithographic processes during PCB fabrication, making them a more reliable basis for the PAM design. Therefore, a CPW would be a suitable transition line for the PAM. [4]

In addition, a CPW has lower losses compared to a simple microstrip due to differences in the electric field distribution, as illustrated in Figure 5.

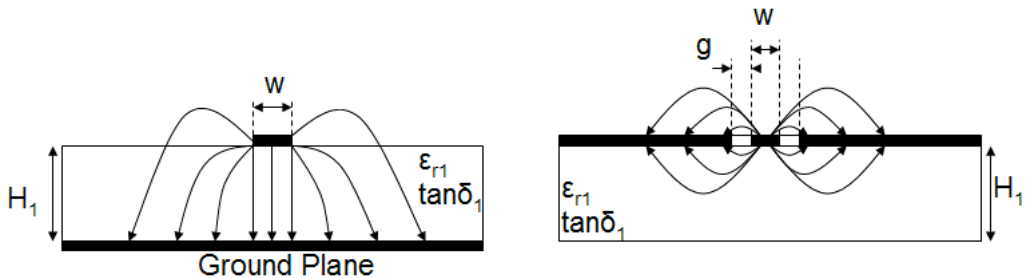


Figure 5: Electric field lines of a microstrip (left) in comparison to a CPW (right). The picture was taken from a thesis from Papió [5].

In a CPW, the electric field is evenly distributed between the air and the substrate. Since air is nearly lossless and the field does not penetrate as deeply into the substrate, attenuation is minimized. [4]

2.2 S-Parameters

Scattering parameters (S-parameters) are an important quantity to describe how much energy passes through an electric network. They are defined as

$$S_{ij} = \frac{V_i}{V_j}, \quad (1)$$

where V_i is the input voltage at port i and V_j is the output voltage at port j. For a two-port network, there are four S-parameters: S_{11} , S_{22} , S_{21} and S_{12} . The latter two, also

known as insertion loss, describe signal transmission between the ports. S21 represents the fraction of the signal that propagates from port 1 to port 2, while S12 describes the transmission of the signal from port 2 to port 1. Lower values of S21 and S12 suggest higher losses. S11 and S22 quantify the amount of the incoming signal that is reflected back at ports 1 and 2, respectively. These values, referred to as return loss, should be as low as possible to minimize signal reflections and ensure efficient power transfer. [6]

Frequently, S-parameters are specified in decibels (dB) [6] as

$$20 \cdot \log_{10}\left(\frac{V_i}{V_j}\right) \text{ dB}. \quad (2)$$

2.3 Evaluation of a Previous Prototype and Trace Modeling

For the simulation of the first prototype, which only includes a CPW, Ansys HFSS 2023 R2 (High-Frequency Structure Simulator) was used. The starting point for the HFSS model was the CPW of a previous prototype that had been designed using an online impedance calculator. In addition to the CPW, this earlier design already incorporated an amplifier, a bias tee, and several gain equalizers. However, measurement of the S-parameters, shown in Figure 6, revealed suboptimal performance. To determine whether the issues with the S-parameters originated from the CPW or from the components, a simulation of the signal trace of this previous prototype was necessary.

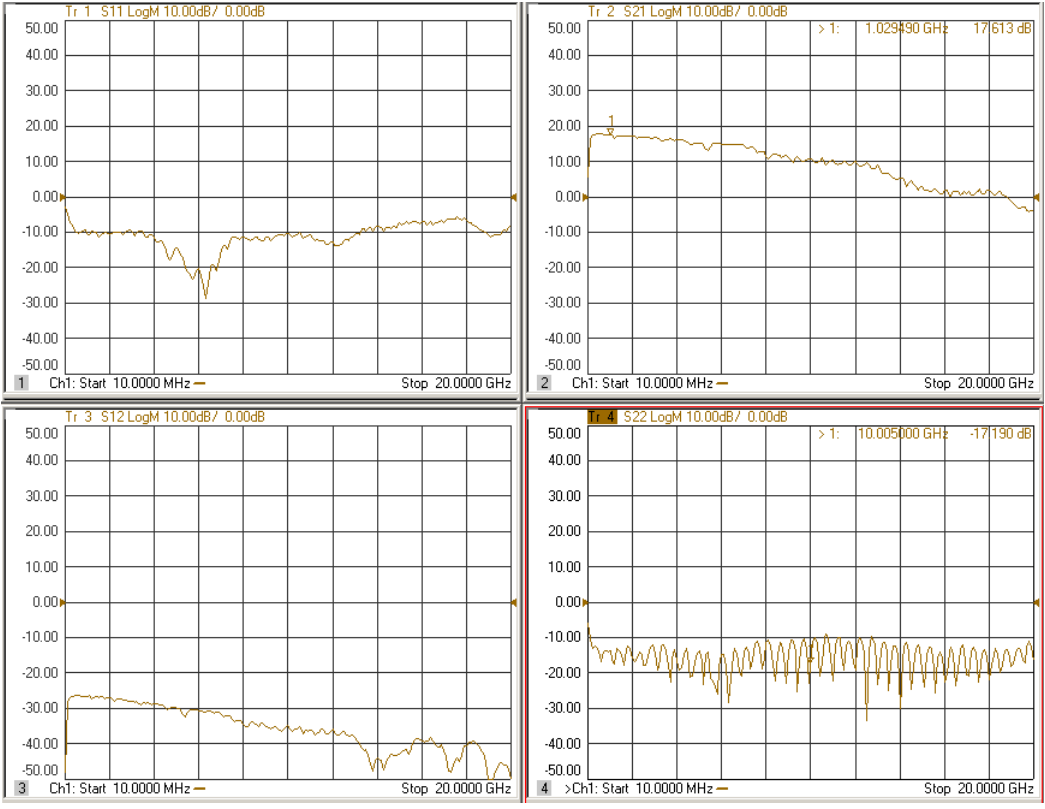


Figure 6: S-Parameter measurement of a previous prototype for the PAM, that includes a CPW, one amplifier, a bias tee and three equalizers. The figure was taken from the GitHub page of the HCRO [3].

Throughout the frequency range of 0.01–20 GHz, the S21 parameter declines by about 20 dB rather than remaining near the expected amplification of 20 dB. In addition, the curve exhibits ripples, particularly at higher frequencies, suggesting the presence of small resonances. The S11 parameter remains close to or below -10 dB for frequencies between 0.5 and 14 GHz. This indicates moderate impedance matching, since roughly 10% of the signal power is reflected. However, above 14 GHz, S11 increases to almost -5 dB, which means that approximately 32% of the signal power is reflected. In contrast, the S22 parameter remains below -10 dB across the entire frequency range. This could be attributed to the gain equalizers, as they could absorb reflected power after the amplifier. The S12 parameter remains fairly low over the entire frequency range, as not much of the signal is leaking back through the amplifier.

To further investigate the performance issues of this former prototype, an HFSS model of the CPW was created, which is shown in Figure 7.

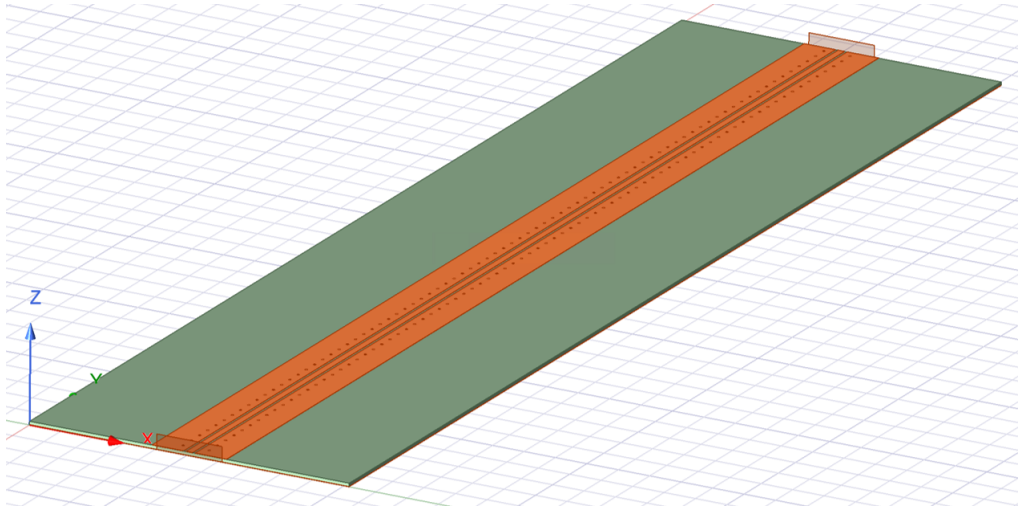


Figure 7: HFSS model of the CPW from a previous prototype.

The signal line and ground planes at the top and bottom of the PCB are defined as copper, while the substrate is specified as Rogers RO4350. The surrounding medium is set to air, and the wave ports at both ends of the PCB are assigned an impedance of 50 ohms. To ensure proper grounding, the top and bottom copper planes are connected using copper cylinders. The dimensions of the CPW are listed in Table 1.

parameter	value [mm]
trace width w	1.04
gap width g	0.4
ground width w_1	5

Table 1: CPW dimensions from previous prototype

The result of the simulation is shown in Figure 8.

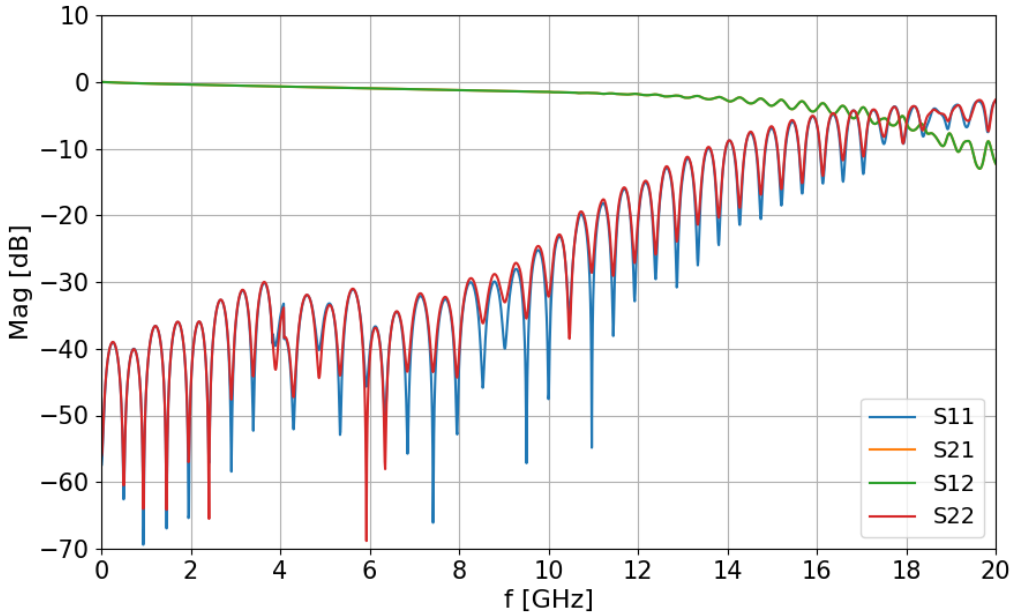


Figure 8: S-parameter simulation of CPW from previous prototype: S11 (blue), S22 (red), S21 (orange) and S12 (green).

Since no amplifier was included in the simulation, the S21 parameter starts at 0 dB. Similar to the measurement, it declines by approximately 13 dB over the frequency range, with noticeable ripples at higher frequencies. The higher losses of the measured S21 parameter are probably due to the components that this prototype contains. The S11 parameter also follows a similar trend to the measurement. It remains below -10 dB up to around 14 GHz before increasing to approximately -3 dB at higher frequencies. The simulated S12 and S22 parameters are almost identical to the S21 and S11 curves, respectively, given the symmetric nature of the CPW structure.

In summary, the simulation confirms the poor performance of the CPW, with only about 5% of the signal passing through at high frequencies. This highlights the need for optimization, which will be addressed in the next section.

2.4 Optimization of the Signal Trace for the First Prototype

To enhance the S-parameters of the CPW model in HFSS, several optimizations were performed for the trace width w and the gap width g . The optimization goals were set to $S22 \leq -20dB$ and $S11 \leq -20dB$, each assigned an equal weight of 1. For the

optimization process, the Genetic Algorithm (Random Search) and the Quasi Newton (Gradient) method were used, both of which yielded similar results. In addition, different initial values for w and g were tested, obtained from the built-in impedance calculator in Altium Designer. To address a small resonance observed around 16 GHz, the width of the top ground planes w_1 was increased to 7.5 mm. Finally, the robustness of the optimized design was tested by slightly varying w and g to assess its sensitivity to manufacturing tolerances. The result of the optimization process can be seen in Figure 9. Its parameters, rounded to four digits, are shown in Table 2.

parameter	value [mm]
trace width w	0.5379
gap width g	0.1143
ground width w_1	7.5

Table 2: optimized CPW dimensions

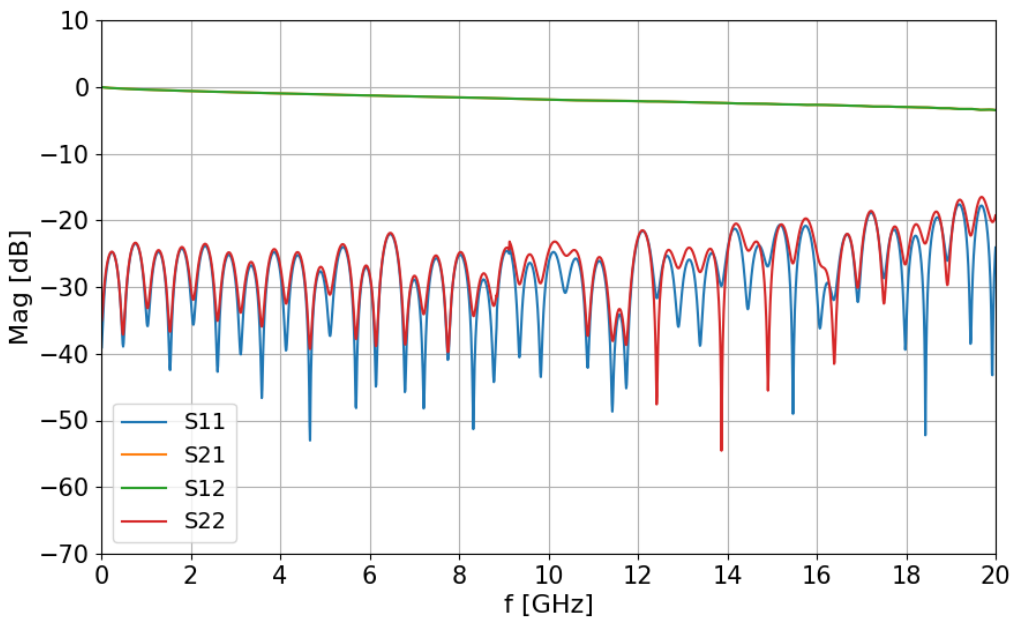


Figure 9: S-parameter simulation of the CPW with optimized dimensions: S11 (blue), S22 (red), S21 (orange) and S12 (green).

Compared to Figure 8, the S-parameters of the optimized CPW show a significant improvement. Both S11 and S22 stay below -20 dB up to 17 GHz and do not exceed -15 dB

across the entire frequency range. Meanwhile, S21 and S12 are fairly smooth with a low gradient, indicating a less lossy and more stable signal path.

2.5 Prototype and Experimental Results

After optimizing the signal trace, the design files for the first prototype were generated using Altium Designer 24 and sent to a PCB manufacturer. The measurement setup for this prototype is illustrated in Figure 10.

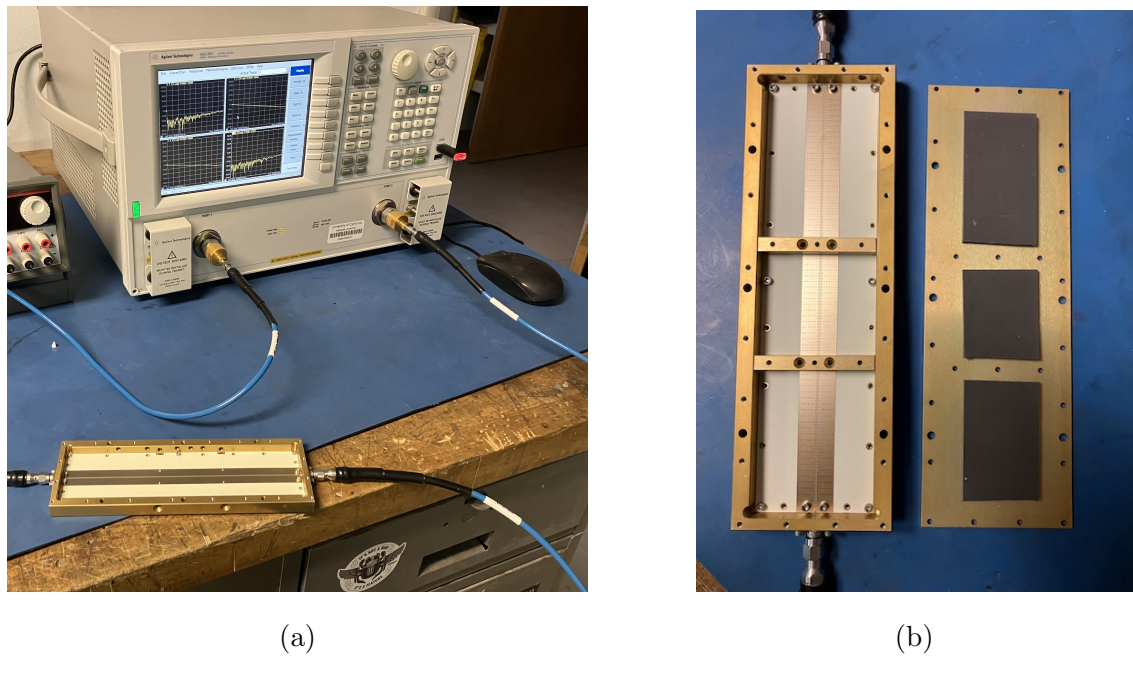


Figure 10: (a) measurement setup: CPW prototype connected to VNA (b) CPW prototype in enclosure with absorbers on the inside of the lid.

Figure 10a shows the prototype CPW connected to the Vector Network Analyzer (VNA). A closer view of the prototype inside the PAM enclosure is shown in Figure 10b. The enclosure features two metal barriers, which prevent signals that radiate out of the trace at the beginning from coupling back in at the end. To further minimize interference from internal radiation, RF absorbers are placed on the inside of the lid. Although the lid remains closed when the PAM is integrated into the antenna, opening it during measurements has little impact on the results.

Before measurements were made, the Vector Network Analyzer (VNA) was software calibrated. S21 and S12 were normalized, while S11 and S22 were already close to -20 dB.

Figure 11 compares the measurement results with the optimized simulation from Section 2.4.

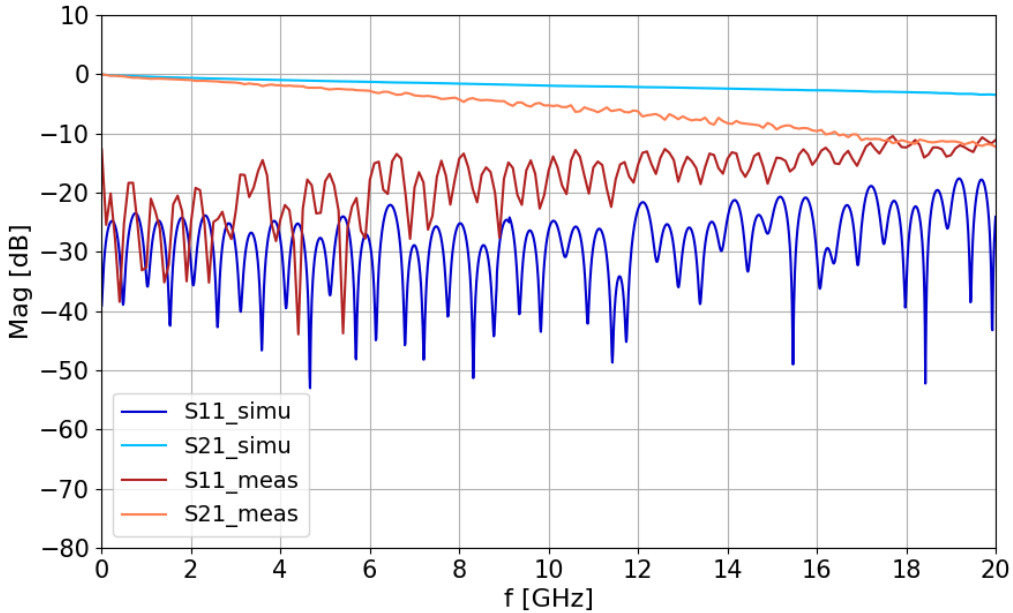


Figure 11: Comparison of CPW prototype measurement (blue) with the CPW simulation results (red).

The measurement results indicate a rather good performance. The S21 parameter (orange) exhibits a smooth decline without significant dips, suggesting minimal unexpected losses. The S11 parameter (red) remains below -10 dB across the entire frequency range, indicating good impedance matching.

In general, simulation and measurement exhibit similar trends. However, the measured performance is slightly worse than the simulated results. This discrepancy could be attributed to several factors, including manufacturing tolerances, material imperfections, or the soldering of the SMA connectors, which were not taken into account in the simulation model.

2.6 Summary

In this chapter, the CPW for the PAM was designed, simulated, and measured. The CPW of a previous prototype was analyzed and optimized using HFSS, with the final dimensions summarized in Table 2. Measurement results confirmed that the optimized

CPW performs well, with the S21 parameter remaining below -10 dB across the entire frequency range of 0.01 to 20 GHz. Given these promising results, the optimized CPW will be implemented in future prototypes.

3 Selection of an Appropriate Amplifier

This chapter discusses the second prototype of the PAM, which, in addition to the CPW, incorporates an amplifier. Two different versions of this prototype were developed to evaluate the performance of two different amplifiers. The chapter first outlines the design process, followed by the measurement results of the manufactured prototypes.

3.1 Design of the HMC462-Based Prototype

The first version of the second prototype incorporated an Analog Devices HMC462 amplifier, which had previously demonstrated good performance in an RF switch design. This amplifier provides a gain of 13 dB and operates in a frequency range of 2–20 GHz [7]. The layout of the prototype including the HMC462 amplifier, is shown in Figure 12.

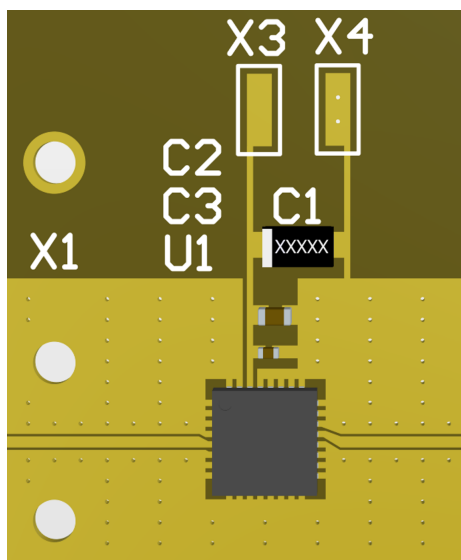


Figure 12: Prototype design including HMC462 amplifier.

To ensure stable operation, the design includes three bypass capacitors, as recommended by the manufacturer [7]. These capacitors help filter out alternating current (AC) noise from the supply voltage by providing a short for AC to ground. The wires for the supply voltage of +5 V and ground will be soldered on pads X3 and X4, respectively. Since the amplifier chip already integrates DC-blocking capacitors, additional coupling capacitors

were not required on the signal trace before or after the amplifier.

The transitions between the CPW and the amplifier pads were modeled in HFSS, as illustrated in Figure 13.

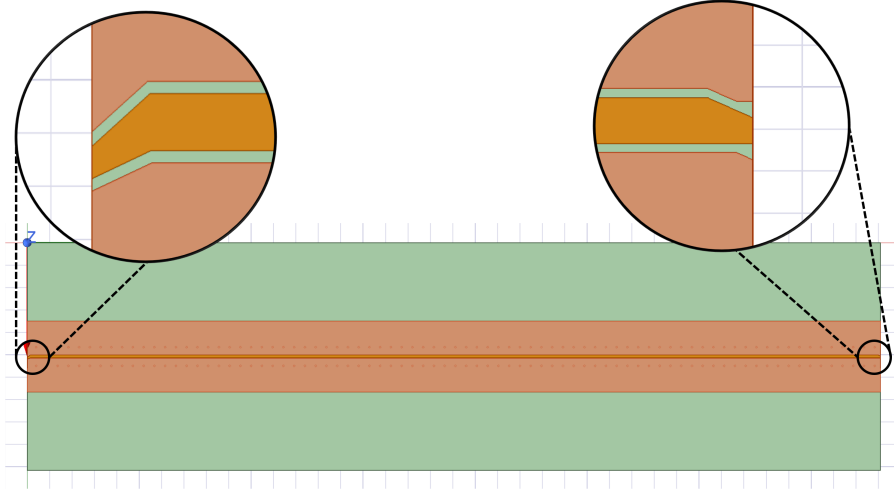


Figure 13: HFSS model of transitions to HMC462 amplifier.

To minimize signal loss and impedance mismatches, the transition angles were kept below 40° , as suggested by a study on CPW to microstrip transitions [8]. The simulation focused on the signal trace and the transitions, excluding the amplifier itself. However, connecting both transitions with a simple line would significantly affect the result, due to the narrowing and different vertical positions of the transitions. Thus, the transitions were modeled at the beginning of the trace, each oriented with its narrow end facing the port.

Figure 14 compares the simulation results of the transition design with those of the optimized CPW from Section 2.4.

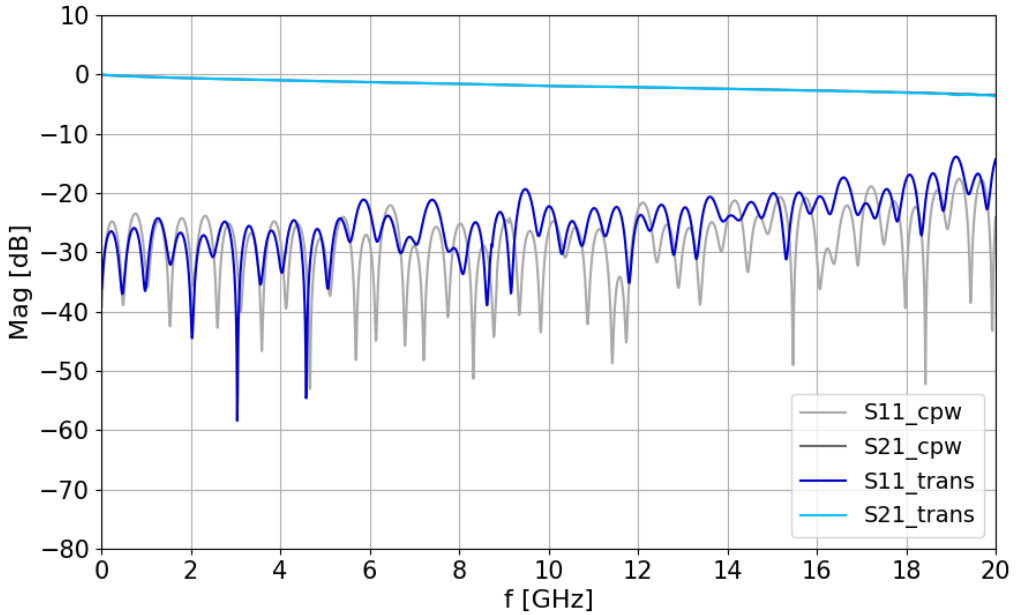


Figure 14: Simulation of CPW with transitions to HMC462 (blue) compared to the simulation of only the CPW (gray).

The differences are minimal: the S21 parameter remains nearly identical. The S11 parameter shows slight degradation, particularly between 6–12 GHz and above 16 GHz. Overall, the transitions do not appear to introduce significant issues.

3.2 Design of the MML098GQ4A-Based Prototype

The second version of this prototype includes the Miller MMIC amplifier MML098GQ4A. It provides a higher gain of 23 dB and a slightly wider frequency range of 0.05-20 GHz than the HMC462 amplifier [9]. The higher gain could save costs and space for the new PAM, as fewer amplifiers would have to be included. The layout of the prototype is shown in Figure 15.

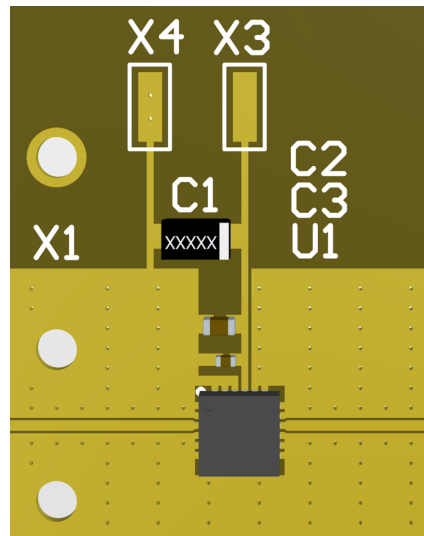


Figure 15: Prototype design including MML098GQ4A amplifier.

In this design, the coupling capacitors on the signal trace before or after the amplifier were missing. To accommodate those capacitors on the PCB, the signal trace had to be cut manually using a razor.

As with the first version, the transitions between the signal path and the amplifier pads were modeled in HFSS. The corresponding model is shown in Figure 16.

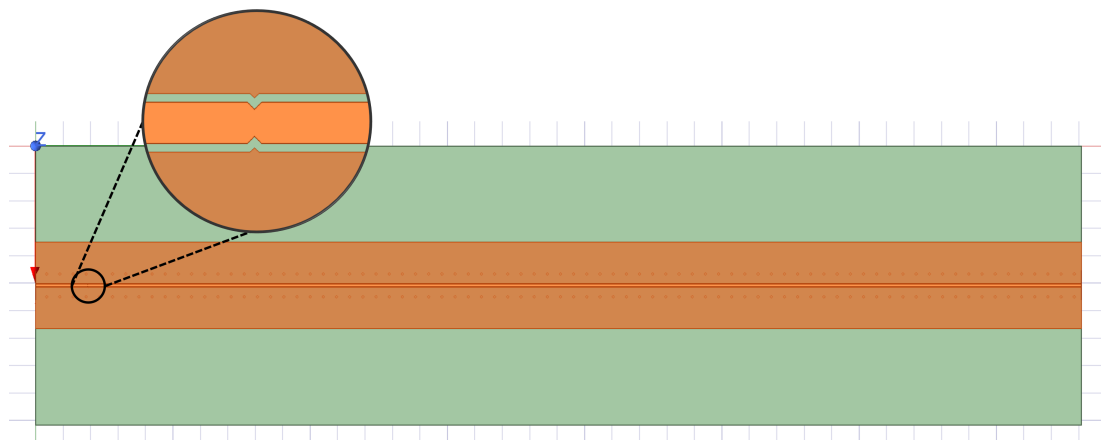


Figure 16: HFSS model of transitions to MML098GQ4A amplifier.

Since this time the transitions were at the same vertical position, they could be directly connected.

The simulation results, shown in Figure 17, indicate that the transitions for the MML098GQ4A amplifier do not introduce significant losses.

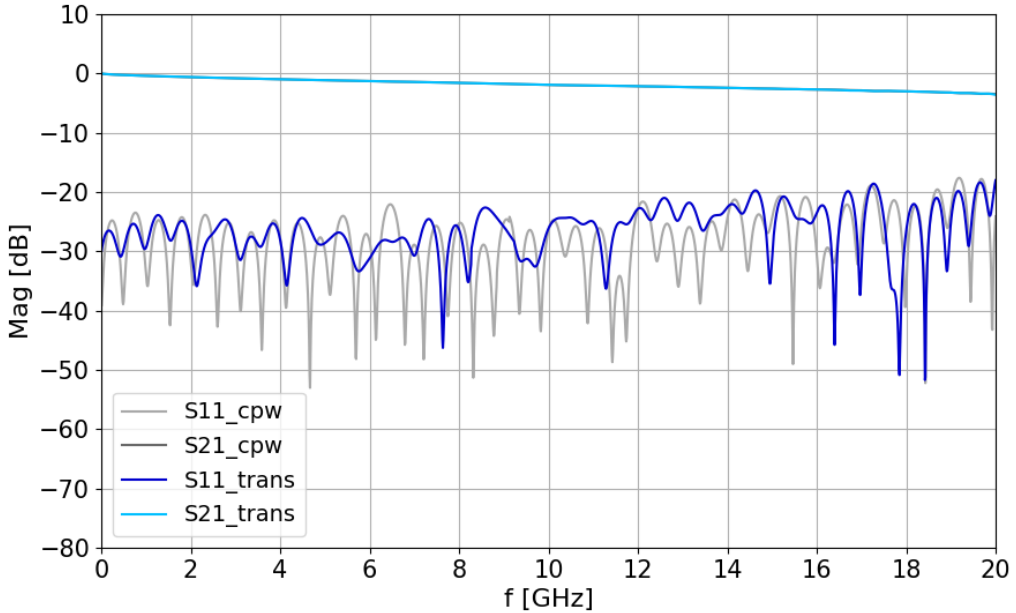


Figure 17: Simulation of CPW with transitions to MML098GQ4A (blue) compared to the simulation of only the CPW (gray).

The S21 parameter remains almost identical to that of the CPW-only simulation and the S11 parameter shows no noticeable degradation. Overall, this transition design appears to perform even better than the one used for the HMC462 amplifier.

3.3 Assembly and Measurement of the HMC462-Based Prototype

After the PCB was manufactured, the components were soldered by hand using a stencil to apply the solder paste, followed by reflow soldering in an oven. A section of the assembled prototype is shown in Figure 18.

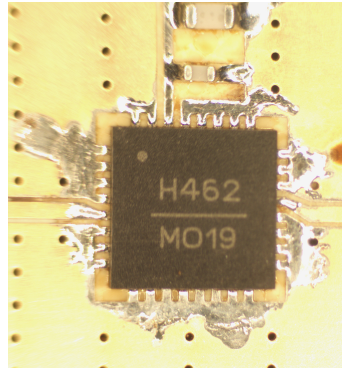


Figure 18: Soldering of HMC462 amplifier.

Although an excessive amount of solder paste was applied, all pins appeared to be well aligned and no shorts were created.

The measurement setup is depicted in Figure 19.

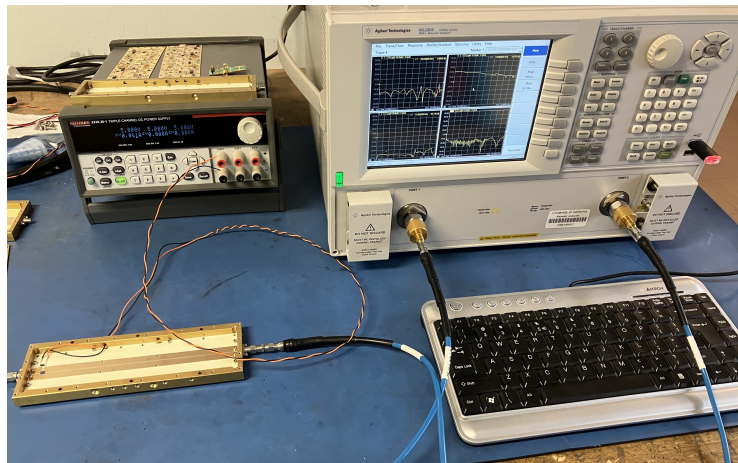


Figure 19: Measurement setup for HMC462-based prototype: prototype (bottom-left) connected to power supply (top-left) and VNA (top-right).

In addition to the Vector Network Analyzer (VNA) on the right-hand side, the setup includes a +5 V power supply for the amplifier. Before measurement, the VNA was software calibrated. The measurement results are presented in Figure 20.

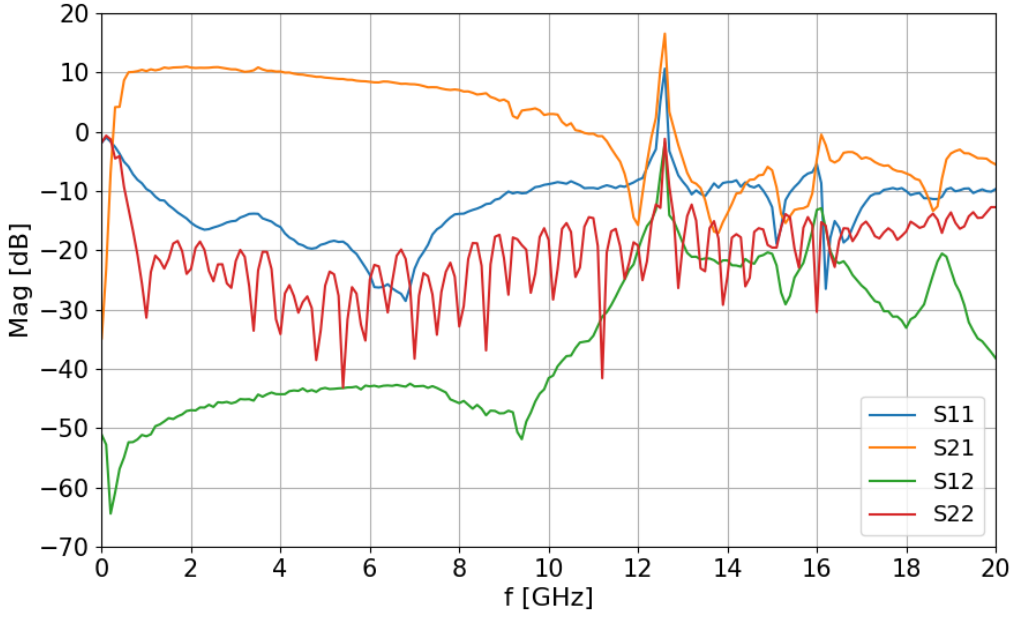


Figure 20: Measurement of HMC462-based prototype: S21 (orange), S12 (green), S11 (blue) and S22 (red).

Overall, the measured S-parameters indicate poor performance. Instead of maintaining the expected amplification of approximately 10 dB, S21 drops by more than 20 dB, exhibiting a zigzag pattern above 10 GHz. This suggests significant losses and resonances. Furthermore, S11 frequently exceeds -10 dB, indicating poor impedance matching. A particularly prominent resonance peak appears around 12.6 GHz across all four S-parameters. The distance from the first SMA connector to the amplifier corresponds to approximately half a wavelength at this frequency. Thus, the issue seems to originate in this region. A possible explanation is a poor solder connection, leading to a standing wave between the SMA connector and the amplifier. This could cause the amplifier to operate in an unstable manner, resulting in excessive gain at this frequency. As a consequence, the S21 parameter exceeds the expected 10 dB amplification, while the S11 parameter rises above 0 dB. However, since the MML098GQ4A-based prototype demonstrated significantly better performance, further investigation of this issue was deemed unnecessary.

3.4 Assembly and Measurement of the MML098GQ4A-Based Prototype

The soldering process for the second amplifier followed the same procedure as the HMC462-based prototype. A section of the solder paste application and the assembled prototype is shown in Figure 21.

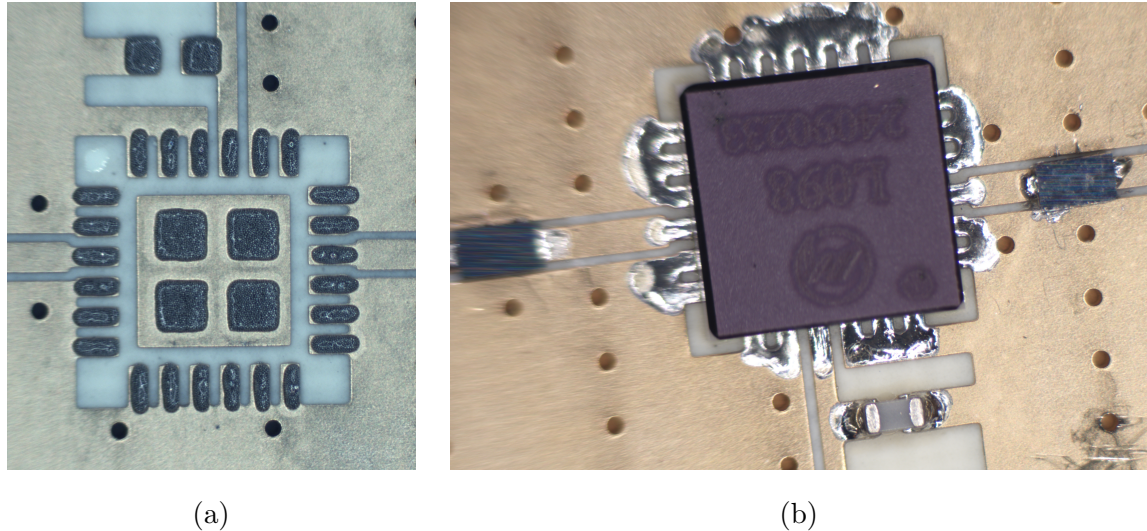


Figure 21: (a) Solder paste application (b) Soldering of MML098GQ4A-based prototype.

This time, a slightly reduced amount of solder paste was applied, resulting in a cleaner assembly. In addition, the coupling capacitors, which the MML098GQ4A amplifier requires, were included.

The measurement setup remained identical to that of the HMC462-based prototype. During initial measurements, a small resonance peak appeared at approximately 16.7 GHz, which seemed to originate from radiation emitted by the amplifier itself. This issue was fixed by applying RF-absorber material on top of the amplifier.

The final measurement result of the MML098GQ4A-based prototype, compared to the CPW prototype from Section 2.5 is shown in Figure 22.

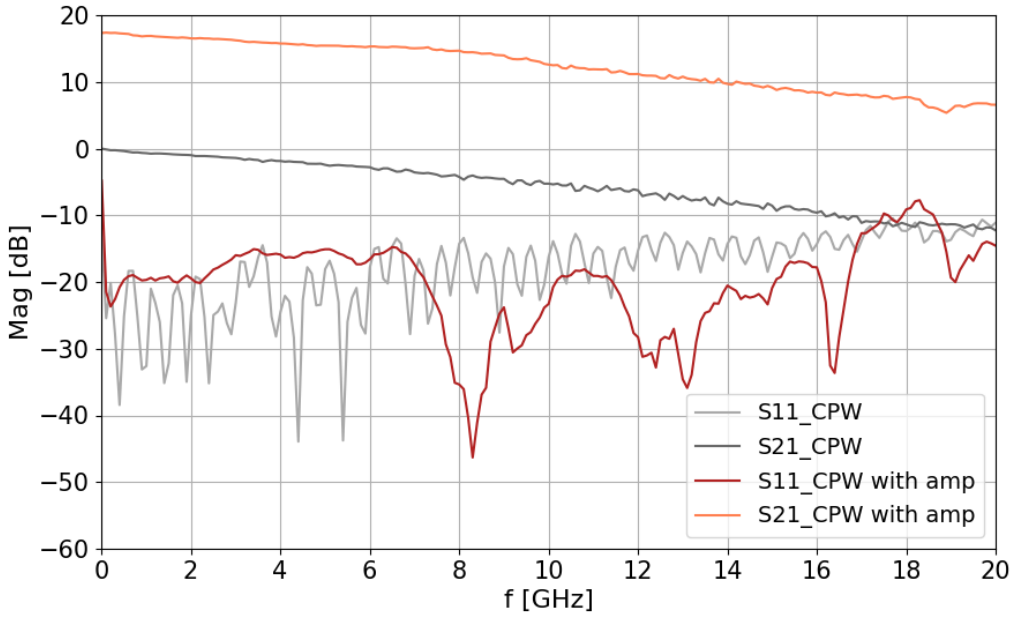


Figure 22: Measurement results of the MML098GQ4A-based prototype (red) compared to the CPW-only prototype (gray).

In general, the S-parameters of the MML098GQ4A-based prototype show only minor degradation compared to the CPW prototype. The S₁₁ parameter of the CPW prototype remains below -10 dB across the entire frequency range, whereas the S₁₁ parameter of the MML098GQ4A-based prototype only exceeds this threshold below 0.2 GHz and around 19 GHz. The peak below 0.2 GHz should be related to the amplifier itself, which is only rated down to 0.05 GHz. The S₂₁ parameter of the MML098GQ4A-based prototype remains relatively smooth, with the exception of a small dip around 18.8 GHz. Due to the gain of the amplifier, S₂₁ is about 18 dB higher than that of the CPW prototype throughout the entire frequency range. The amplifier does not introduce much additional slope to the response.

To counteract the negative slope introduced by the trace length, equalizers can be incorporated. To estimate their effectiveness, a single 3.5 dB equalizer was manually added to the prototype by cutting the trace and soldering it in place. The result of this measurement is shown in Figure 23.

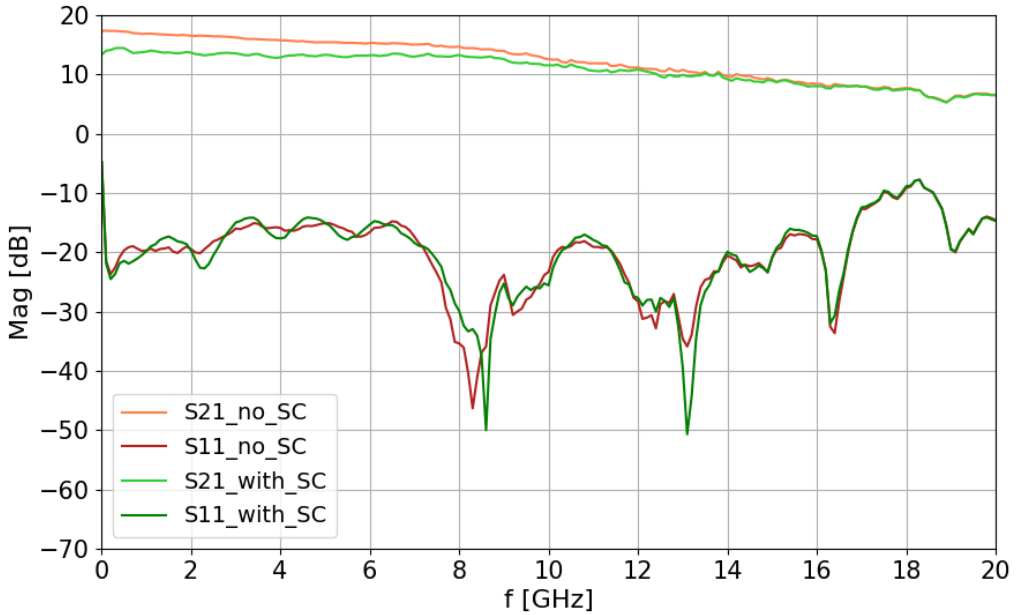


Figure 23: Measurement of MML098GQ4A-based prototype with (green) and without (red) one slope compensator added.

While the equalizer has little impact on the S21 parameter, it successfully compensates for approximately 3.5 dB of the negative slope. Based on this, incorporating three equalizers should be sufficient to fully counteract the total slope of approximately -11 dB.

3.5 Summary

In this chapter, two versions of the second prototype, each with a different amplifier, were designed and measured. Simulation of the amplifier transitions confirmed that their impact on overall performance was negligible. Measurement of the HMC462-based prototype revealed poor performance with significant resonances. In contrast, the MML098GQ4A-based prototype demonstrated much better performance, with S21 remaining below -10 dB across almost the entire frequency range, as shown in Figure 22. Consequently, this amplifier was selected for future designs. In addition, testing with a single 3.5 dB equalizer suggested that the final PAM module should incorporate three equalizers to compensate for the negative slope of the signal trace.

4 Cascading Amplifiers and Attenuators

This chapter presents the third prototype of the PAM, which incorporates three amplifiers and two attenuators. After this design, only a few additional components for power detection remain to complete the PAM module. The chapter begins with an overview of the design process, followed by the measurement results of the assembled prototype.

4.1 Design

The design of the third prototype of the PAM can be seen in Figure 24

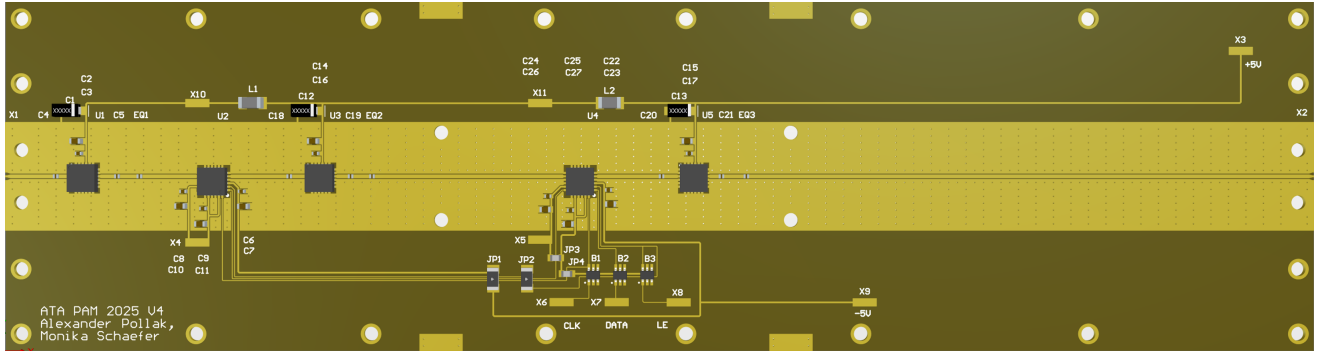


Figure 24: Prototype design including 3 amplifiers (U1, U3, U5) and 2 attenuators (U2, U4).

The design of the third prototype includes three amplifiers (U1, U3, U5) and two variable attenuators (U2, U4) to control the total gain. The alternating arrangement of amplifiers and attenuators prevents excessive voltage levels that could damage the amplifiers. The theoretical gain of the module ranges from 7 dB to 69 dB. However, actual performance is affected by signal losses due to trace length and the presence of equalizers (EQ1–3).

To minimize high-frequency noise emitted by the amplifiers, two ferrite beads (L1, L2) are incorporated into the power supply line. The attenuators require both a positive supply voltage of +5 V and a negative supply voltage of -5 V. In addition, three input signals — clock (CLK), data and latch enable (LE) — are needed to configure their attenuation levels. The data input consists of a 12-bit pattern that specifies the attenuation settings for both attenuators, while the clock signal determines the timing of each bit. The data signal propagates through the first attenuator before reaching the second. After the first 6 bits have passed through the first attenuator, a pulse in the Latch Enable (LE) sig-

nal locks in the current bit pattern, and both attenuators are set to the desired mitigation.

To ensure compatibility with the existing enclosure of the 2007 PAM module, the solder pads for all input signals are positioned identically to those of the original PAM. The +5 V supply voltage is routed across the signal trace from X10 to X4 and from X11 to X5 via two soldered wires. Where input signals must cross below the CPW, zero ohm resistors (JP1–4) are used.

To protect the attenuators from excessive voltage, three buffers are included for the CLK, DATA, and LE signals. In addition, bypass capacitors safeguard the entrances of the supply voltage, ensuring stable operation.

To optimize the transition between the SMA connector and the signal trace, four different transition designs were modeled in HFSS, as shown in Figure 25.

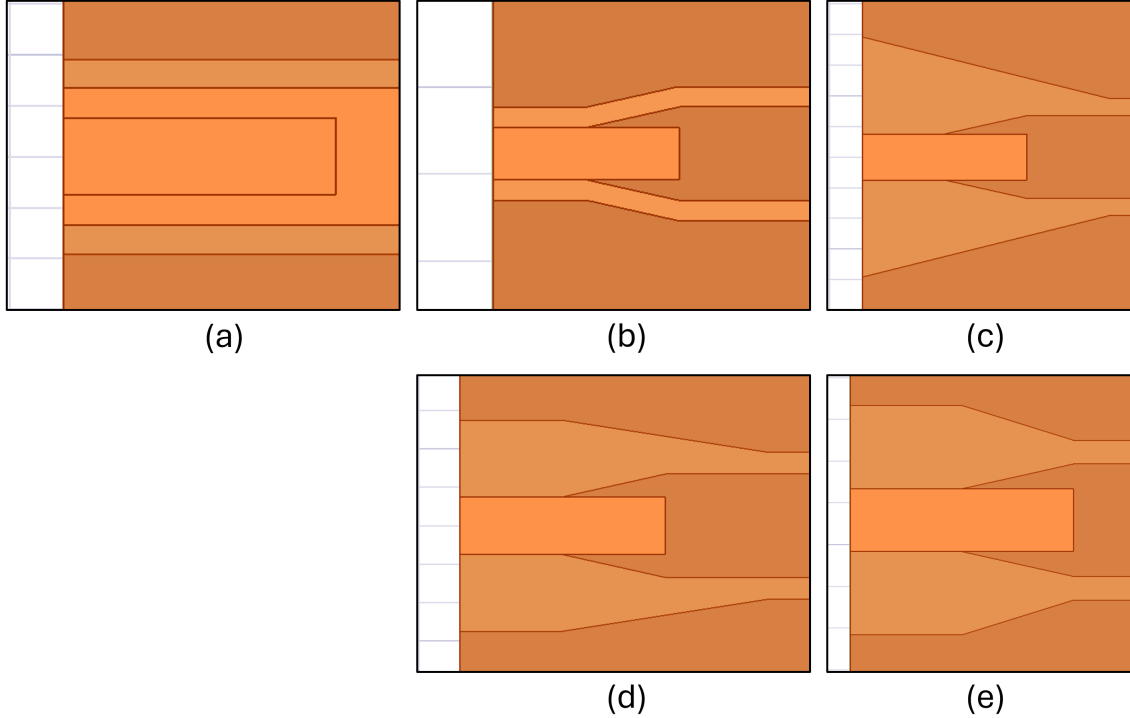


Figure 25: (a) SMA pin on CPW without any transition, (b - e) some possible shapes for SMA pin to CPW transitions.

The soldering of the SMA pin was simulated by incorporating a cuboid, its length and width matching the actual pin dimensions and its height corresponding to its position

above the signal trace. The gap width at the entrance (except for (a)) was determined using the Altium Impedance Calculator, ensuring proper impedance matching for a CPW with the given pin dimensions. To facilitate soldering of the SMA pin, the trace already widens after half the length of the SMA pin. Among the four designs, the bottom-right transition exhibited the best performance and was selected for this prototype.

Furthermore, a comprehensive HFSS model was created to include all necessary transitions of the prototype. As shown in Figure 26, this model incorporates two SMA transitions, three amplifier transitions, and two attenuator transitions.

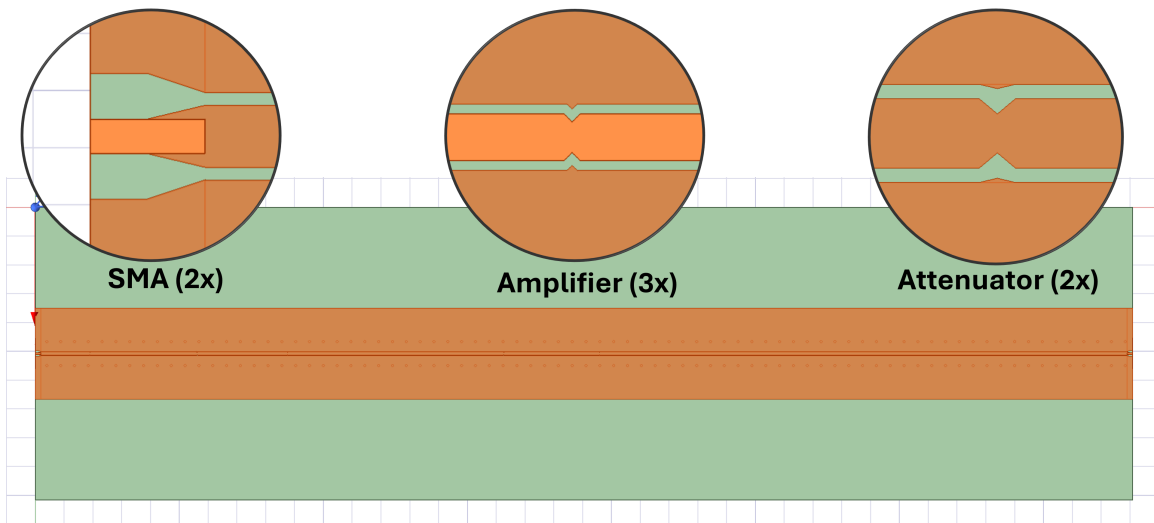


Figure 26: HFSS model including all transitions for SMA connectors, amplifiers and attenuators.

The simulation results, compared to a CPW-only model, are presented in Figure 27. The CPW-only model includes the SMA pin shown in Figure 25a on both ends.

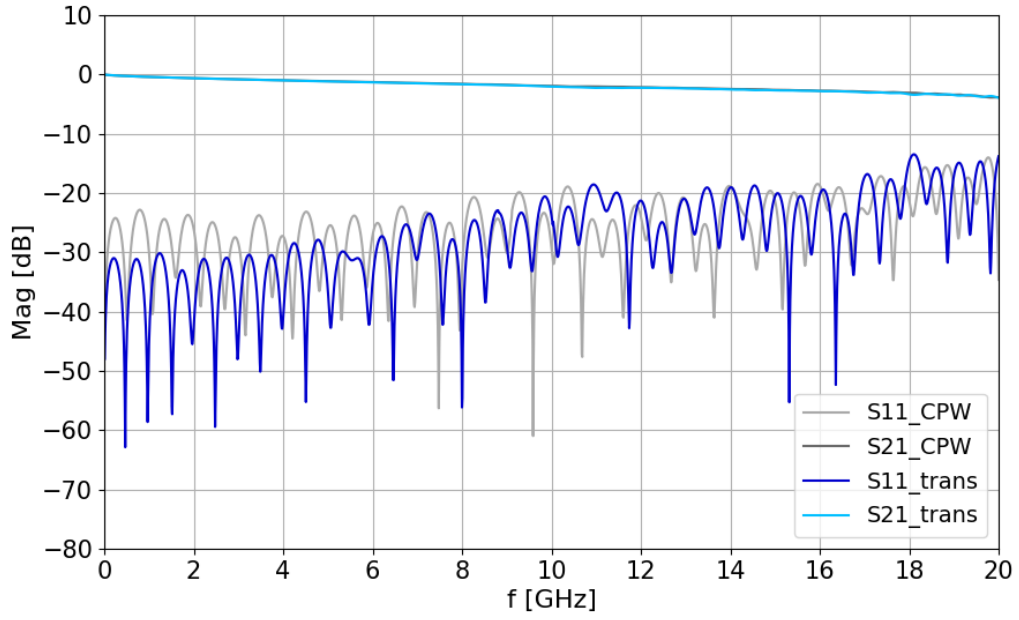
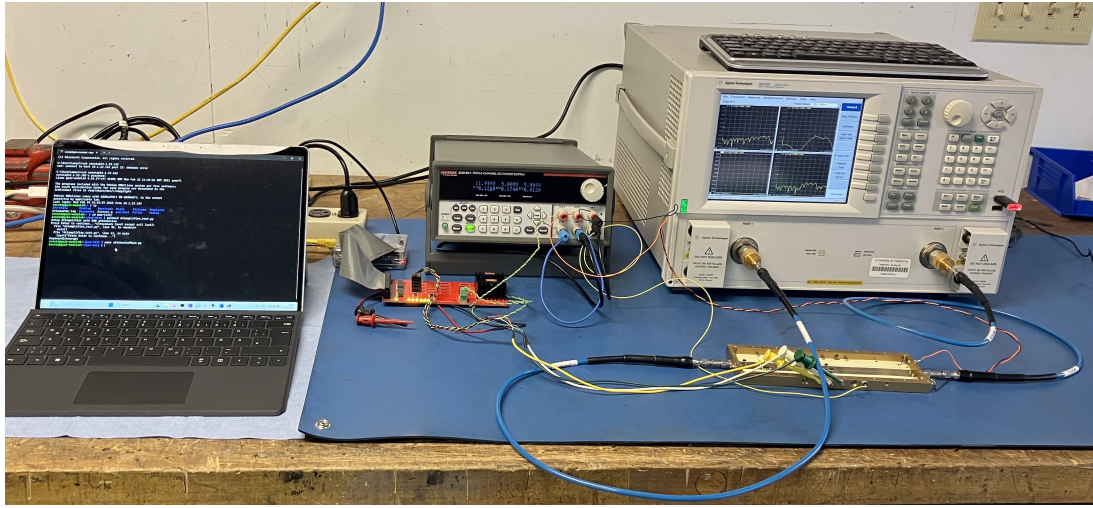


Figure 27: Simulation of CPW with all transitions (blue) and CPW with SMA pin only (gray).

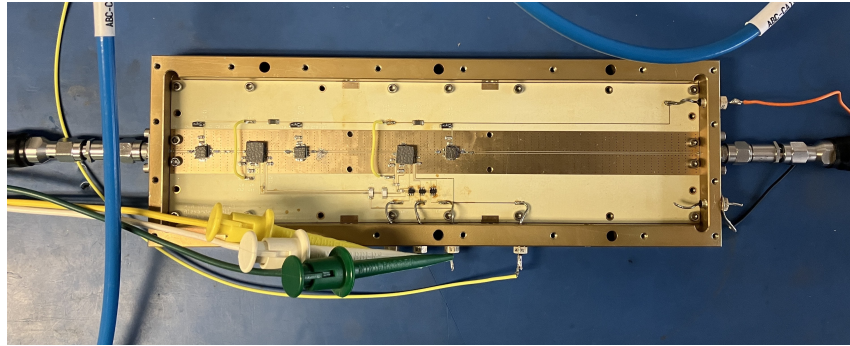
In general, the inclusion of transitions slightly enhances performance. The S11 parameter of the CPW with transitions performs very similar at frequencies above 10 GHz. At lower frequencies, it is slightly better because of the smoother transition to the SMA connector. The S21 parameter of both models looks almost identical, exhibiting only minor ripples at higher frequencies.

4.2 Measurement

Figure 28 shows the measurement setup for the manufactured and assembled prototype.



(a)



(b)

Figure 28: (a) Measurement setup: prototype connected to VNA (right) and power supply (middle), computer with rasbery pi and red control board for attenuation control (left). (b) Close-up of Prototype.

Figure 28a illustrates the measurement setup, while Figure 28b provides a close-up view of the prototype. On the left-hand side of Figure 28a, a computer running a Python script was used, together with a Raspberry Pi and a red control board, to adjust the attenuation levels. The power source in the center of the picture supplied the voltages required for the prototype and the Raspberry Pi. On the right-hand side, the prototype itself and the Vector Network Analyzer (VNA) were positioned. Before measurement, the VNA was software calibrated.

Figure 29 shows the measured S11 and S21 parameters of the prototype for attenuation settings of 7 dB, 27 dB and 69 dB.

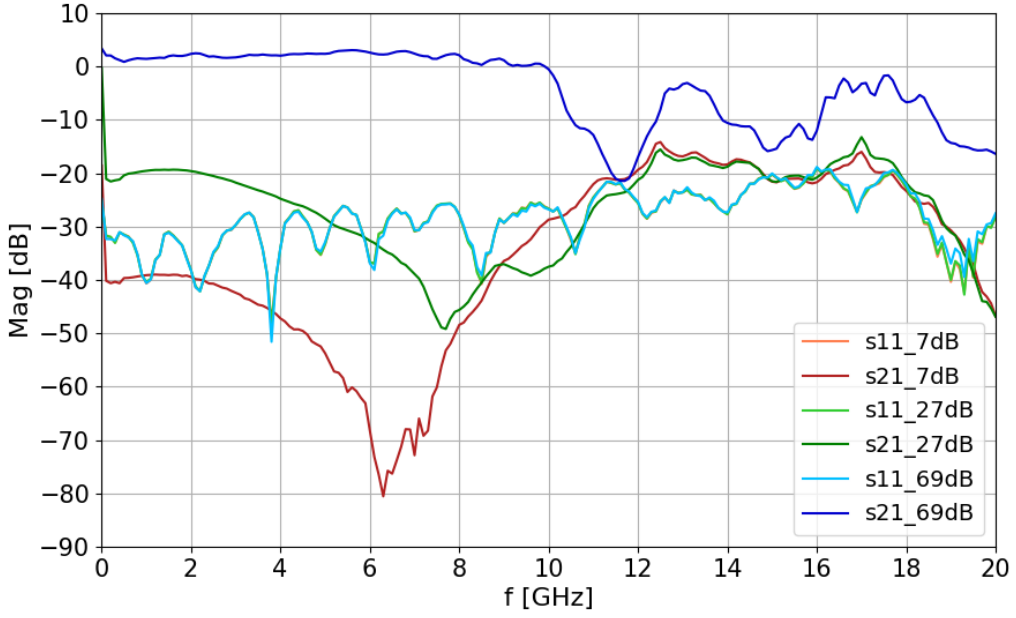


Figure 29: Measurement results of 3rd prototype. Due to different attenuation settings the theoretical values of the S21 parameter should equal 7 dB (red), 27 dB (dark green) and 69 dB (dark blue). However, -20 dB connectors, a VNA output level of -10 dB, and a slightly lower than expected amplifier gain reduce the theoretical gain by approximately 45 dB. The S11 parameters for the different attenuation settings 7 dB, 27 dB and 69 dB are orange, light green and light blue, respectively.

The S21 parameters of the measurement show two major issues. First, they do not seem to respond reliably to the attenuation settings, even at lower frequencies. Secondly, they show increased variations at higher frequencies. In contrast, the S11 parameters remain nearly identical across all attenuation settings and consistently stay below -20 dB, suggesting that the issues are not related to the SMA connectors.

To protect the VNA from excessive voltage, its output level was reduced to -10 dB and -20 dB SMA adapters were used. In addition, the MML098GQ4A amplifier exhibits a gain about 5 dB lower than the manufacturer's specifications [9], as seen in Figure 22. Consequently, the measured gain should be around 45 dB lower than the theoretical total amplification. This expectation applies to the S21 parameter of the 7 dB (red) and 27 dB (dark green) curves at lower frequencies. The S21 parameter for the 69 dB curve (dark blue) is expected to be approximately 40 dB higher than the 27 dB graph (dark green).

This had been observed in earlier measurements. However, re-soldering of components and wires might have introduced excessive voltage — potentially due to an unintentional short circuit or electrostatic discharge — causing damage to the attenuators.

Another possible reason for unexpected attenuation levels is incorrect signal timing between the attenuators. To investigate this, the clock and data input signals at the entrance of both attenuators were measured with an oscilloscope, as shown in Figure 30.

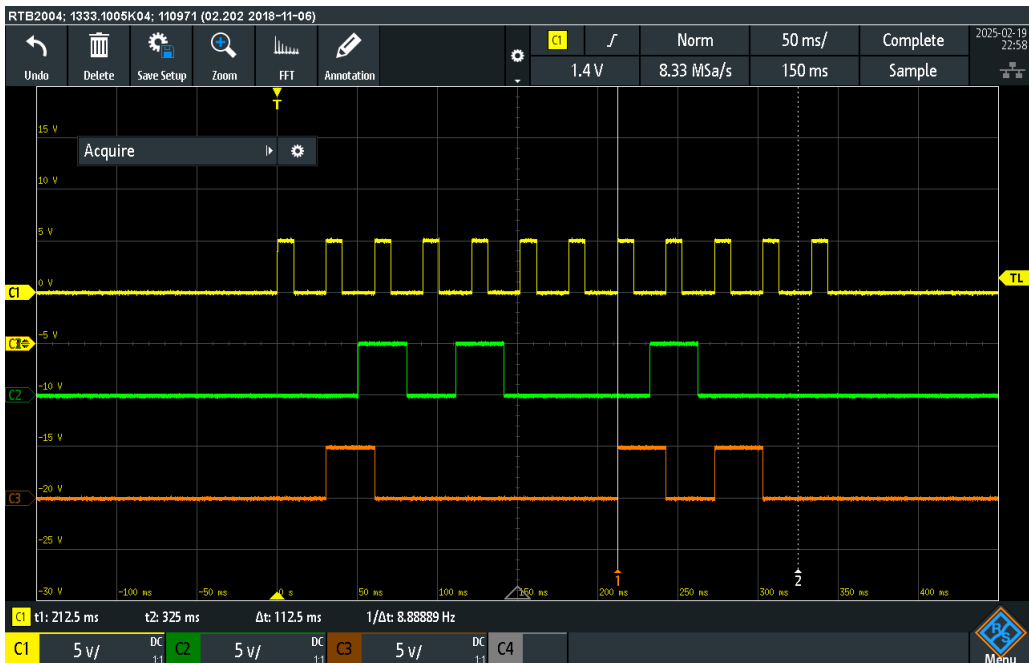


Figure 30: Measurement of PAM V4 attenuator signals with an oscilloscope: input clock signal for both attenuators (yellow), input data signal for first attenuator (green), input data signal for second attenuator (orange).

On every rising edge of the clock signal (yellow), the attenuators read the current state of the data signal. The data input of the first attenuator (green) is always in a well-defined state when the clock signal increases. However, the data input of the second attenuator (orange) increases simultaneously with the clock signal, potentially resulting in undefined behavior. This issue arises because the first attenuator introduces an additional delay of half a clock cycle to the data signal before passing it to the second attenuator.

Beyond attenuation discrepancies at lower frequencies, the measured S21 curves show strong variations at higher frequencies. Several troubleshooting steps were taken to identify the cause. Replacement of the attenuators improved the low-frequency response, but

did not significantly alter the overall shape of the S21 curves. Removing the equalizers only slightly affected the response by increasing the slope. Testing coupling capacitors with higher capacitance, previously used in the second prototype, had no noticeable effect on the S-parameters. The placement of RF absorber material on the amplifiers and attenuators reduced minor ripples but did not resolve the larger inconsistencies, nor did closing the lid with absorbers on the inside. Cutting the power to each amplifier individually did not indicate a faulty amplifier. The placement of a finger on the power supply line had no impact, ruling out power noise as a major factor.

Initially, excessive radiation within the enclosure seemed the most plausible explanation for the poor performance of this prototype. With nearly 70 dB gain at frequencies up to 20 GHz, internal electromagnetic coupling could degrade signal integrity. This led to the consideration of a modular design approach, discussed in Section 5, where the PAM components are distributed across multiple smaller enclosures. However, later testing of the attenuator module suggested that the issue might be related to the footprint of the attenuator rather than radiation effects. Despite this, the modular design approach remains preferable, as it minimizes potential radiation problems and simplifies the troubleshooting and maintenance of the PAM.

4.3 Summary

In this chapter, the third prototype of the PAM, which incorporates multiple amplifiers and attenuators, was designed and measured. Various SMA connector transitions were simulated and the most effective design was implemented. In addition, a simulation that included all the transitions for the amplifiers, attenuators, and SMA connectors suggested that their impact on performance would be minimal. However, measurement of the prototype relieved two key issues (see Figure 29). At lower frequencies, the S21 parameter remained close to the expected attenuation, but varied between repeated measurements. At higher frequencies, the S21 parameter exhibited increased fluctuations over the frequency range. The first issue was likely caused by damaged attenuators due to excessive voltage during resoldering or incorrect timing of the data signal, as observed in oscilloscope measurements. The high frequency variations were initially attributed to excessive radiation within the enclosure, leading to the consideration of a modular design approach. However, as discussed in the next section, the footprint of the attenuator may

be the actual cause. Nevertheless, a modular design remains advantageous for minimizing radiation, improving troubleshooting, and simplifying maintenance.

5 A Modular Design Approach

In this chapter, a modular design approach is explored in which the PAM components are distributed across multiple smaller enclosures to improve performance. The chapter begins with an overview of the different modules and their interactions. This is followed by simulations and optimizations of the SMA transitions and ground width. Finally, the design and measurement results of the three essential modules — amplifier, attenuator, and detector — are presented and analyzed.

5.1 Overview of different Modules

Figure 31 illustrates the modular design approach for the PAM.

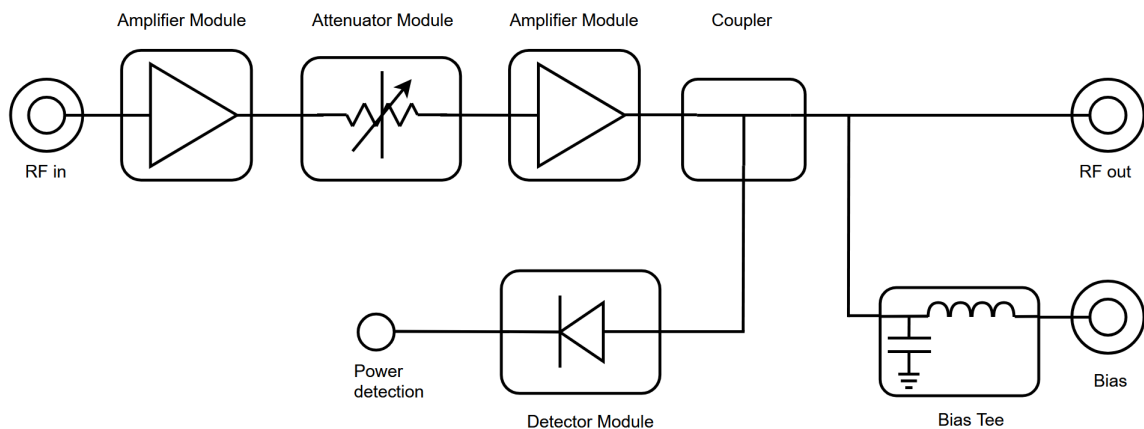


Figure 31: Schematic of modular PAM approach.

The modular PAM consists of five different modules that are connected with SMA cables. Three of those modules - amplifier, attenuator and detector module - are self-designed, while the coupler and bias tee are commercially available components.

Each amplifier module contains a single amplifier with approximately 20 dB of gain to strengthen the incoming RF signal. The attenuator module features a 5-bit attenuator, which allows gain adjustments from 0 to -31 dB. The coupler directs most of the signal to the RF output while diverting about 10 dB to the detector module. The latter measures

signal power using a detector diode, which is essential to properly adjust the attenuator. A bias tee is used to extract the DC component of the RF output, which is required for coax-to-fiber conversion after the PAM.

Using a coupler instead of a traditional power splitter minimizes signal loss for the RF output. Furthermore, as part of the Allen Telescope Array refurbishment program, new feed horns with reduced insertion loss will be installed across all antennas. As a result, two amplifier modules may provide sufficient gain. If more amplification is required, an additional amplifier module can easily be added.

The enclosures for the three self-designed modules are based on a previous RF switch design. Measuring $31.4 \text{ mm} \times 27.4 \text{ mm} \times 9 \text{ mm}$, these enclosures have demonstrated good performance up to 20 GHz.

5.2 Simulations and Optimizations

Since the enclosures for the new modules are significantly smaller than those of previous PAM prototypes, the top ground planes of the coplanar waveguide (CPW) had to be reduced in size. To assess the impact of this change, an optimization of the ground-plane width was performed in HFSS. The optimization was based on the HFSS model used for previous PAM prototypes. Although this model does not precisely represent the absolute values of the new CPW due to differences in length, it is still valid to evaluate the relative impact of ground plane size on CPW performance.

The Adaptive Single-Objective (Gradient) optimizer was used with the condition $S11 \leq -30 \text{ dB}$. To improve efficiency, the optimization was conducted between 10 and 20 GHz, where the S-parameters are most critical. The best and most stable result for small deviations in ground size was obtained for a ground plane width of 2 mm. Figure 32 compares the optimized CPW with the previous CPW with wider ground planes.

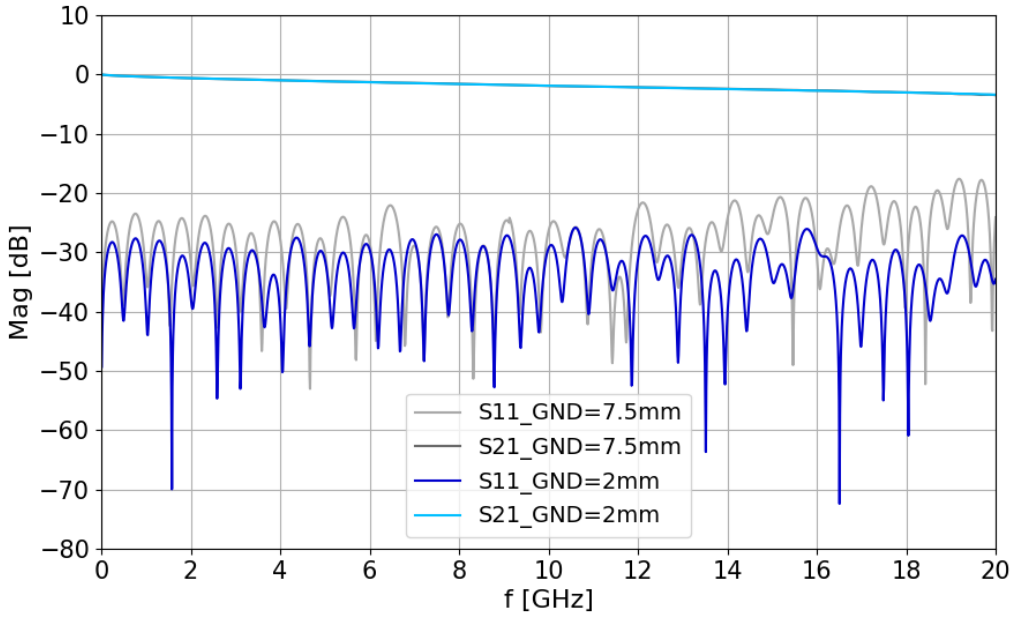


Figure 32: CPW with optimized top ground plane size (blue) compared to previous CPW with wider ground planes (gray).

The S11 parameter of the optimized CPW (blue) remains lower than that of the previous CPW throughout the entire frequency range, indicating reduced losses. Meanwhile, the S21 parameter remains unchanged, confirming that the modification does not negatively affect signal transmission.

In addition to optimizing the width of the ground plane, the transition from the CPW trace to the SMA connectors was also optimized, as shown in Figure 33.

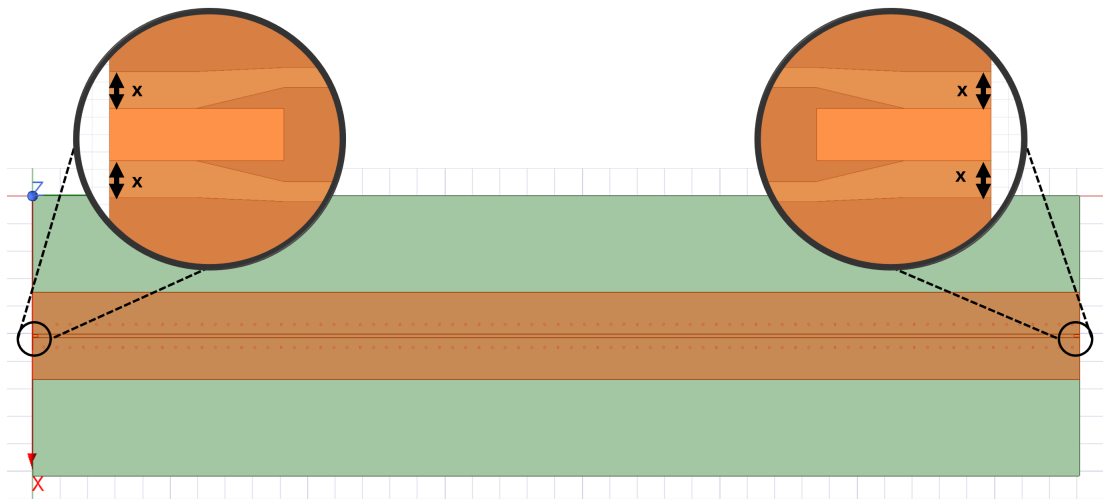


Figure 33: HFSS model for optimizing the SMA-to-trace transition. The optimized parameter is x .

The cuboid at the beginning of the transition resembles the SMA pin. To facilitate soldering, the trace already widens after half the length of the pin. The key parameter optimized in this transition is x , the initial distance between the trace and the ground planes. The Genetic Algorithm (Random search) was used as an optimizer and $S_{11} \leq -20dB$ was defined as a goal. Figure 34 compares the optimization result with a CPW that directly connects to the SMA pin without a dedicated transition.

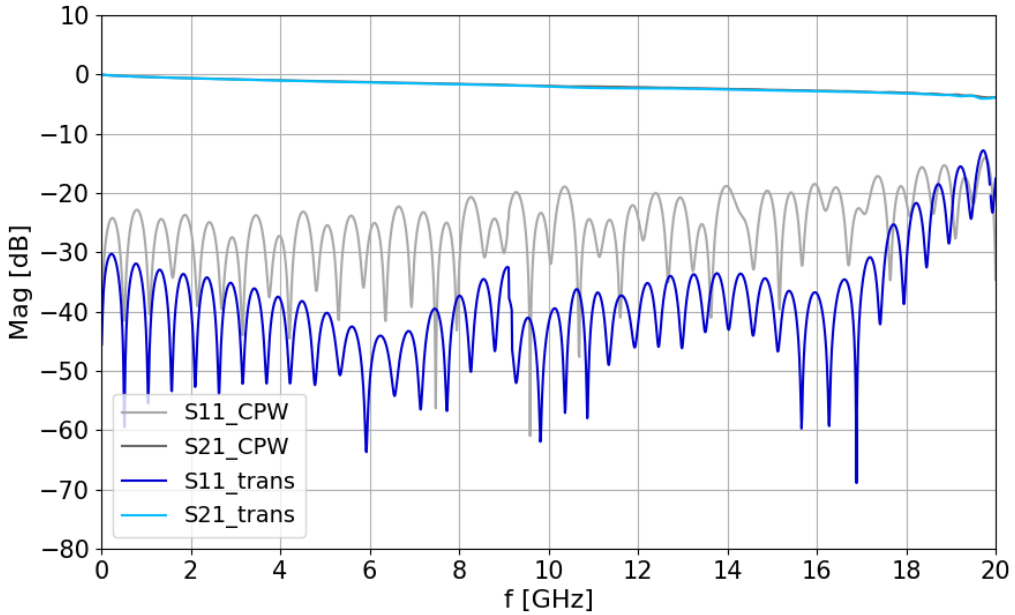


Figure 34: Simulation results comparing the CPW with the optimized SMA transition (blue) to a CPW without a dedicated transition (gray).

The S11 parameter of the CPW with the optimized transition (blue) remains lower than that of the CPW without a transition throughout the entire frequency range, indicating reduced losses. At the same time, the S21 parameter remains unchanged, confirming that the optimization does not introduce additional insertion loss.

5.3 Amplifier Module

The design of the amplifier module, created in Altium Designer, is shown in Figure 35.

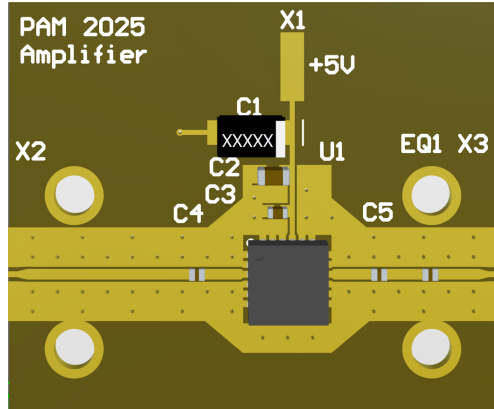


Figure 35: Prototype design of the amplifier module.

The amplifier module features an MML098GQ4A amplifier, accompanied by two 10 nF

decoupling capacitors, an equalizer, and all recommended bypass capacitors to ensure stable operation. SMA connectors are soldered at the input and output of the signal trace (X2, X3), while the solder pad "X1" provides the connection for the +5 V supply voltage. The ground wire can be directly connected to a pin in the conductive enclosure.

Once the PCB was manufactured, all components were reflow soldered using a stencil and an oven. SMA pins and the feedthrough capacitor for the supply voltage were soldered by hand. The fully assembled prototype is shown in Figure 36.

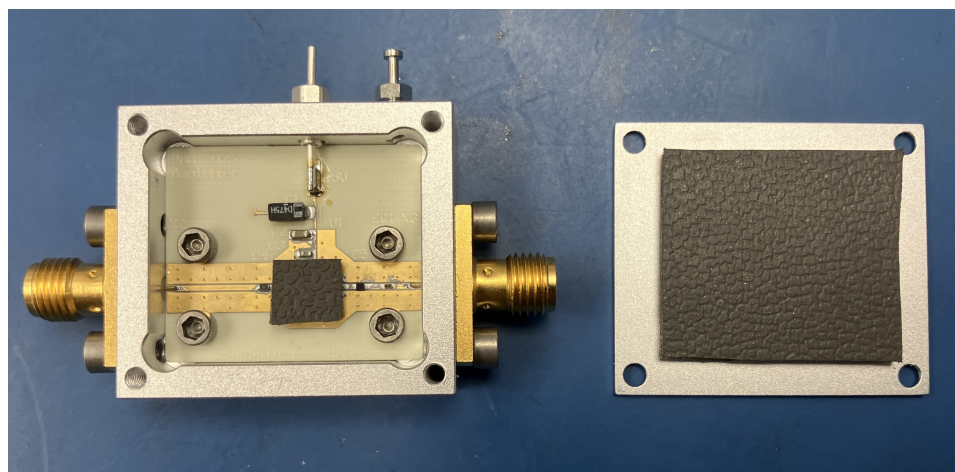


Figure 36: Assembled amplifier module inside the enclosure, with RF absorber material placed on the amplifier and on the inside the lid.

To minimize internal radiation, RF absorber material was placed on top of the amplifier and on the inside of the lid. The measurement setup is the same as for testing the HMC426-based prototype (see Figure 19).

The measurement results are presented in Figure 37.

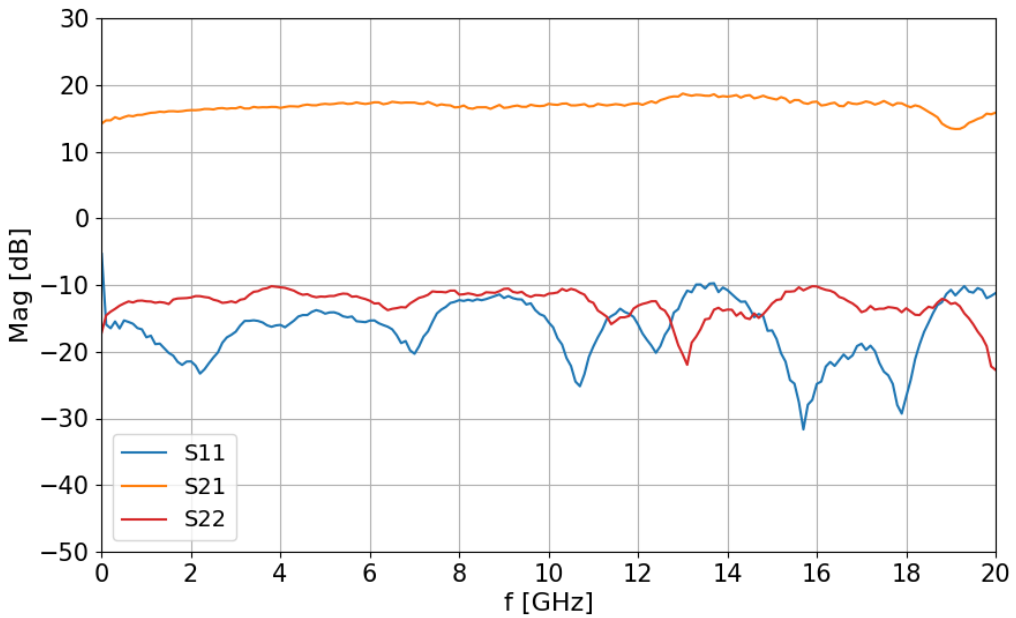


Figure 37: Measurement result of amplifier module: S21 (orange), S11 (blue) and S22 (red).

Overall, the amplifier module demonstrates good performance. The S21 parameter remains stable at approximately 17 dB, with only a single significant dip occurring around 19 GHz. This dip may be attributed to the SMA connectors, which are rated for operation up to 18 GHz. The S11 and S22 parameters remain below -10 dB across the entire frequency range, indicating good impedance matching.

5.4 Attenuator Module

The design of the attenuator module, created in Altium Designer, is shown in Figure 38.

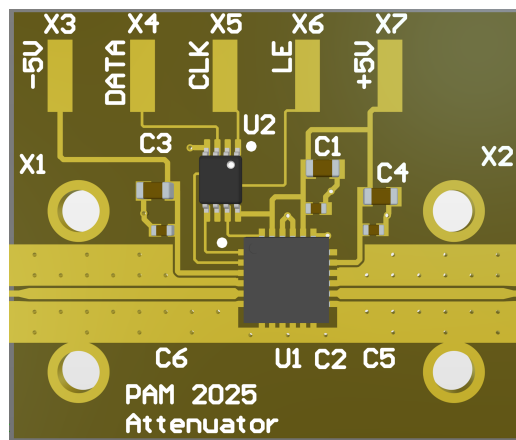


Figure 38: Prototype design of the attenuator module.

The attenuator module includes one HMC1018 attenuator, along with all recommended bypass capacitors and a buffer to protect the amplifier from excessive voltage. SMA connectors are soldered at the input and output of the signal trace (X1, X2). The upper solder pads provide connections to the supply voltages of +5 V (X7) and -5 V (X3) along with control inputs for data (X4), clock (X5) and latch enable (X6). A ground wire can be directly connected to a pin in the conductive enclosure.

The assembly process followed the same reflow soldering procedure as described in Section 5.3. The fully assembled prototype is shown in Figure 39.

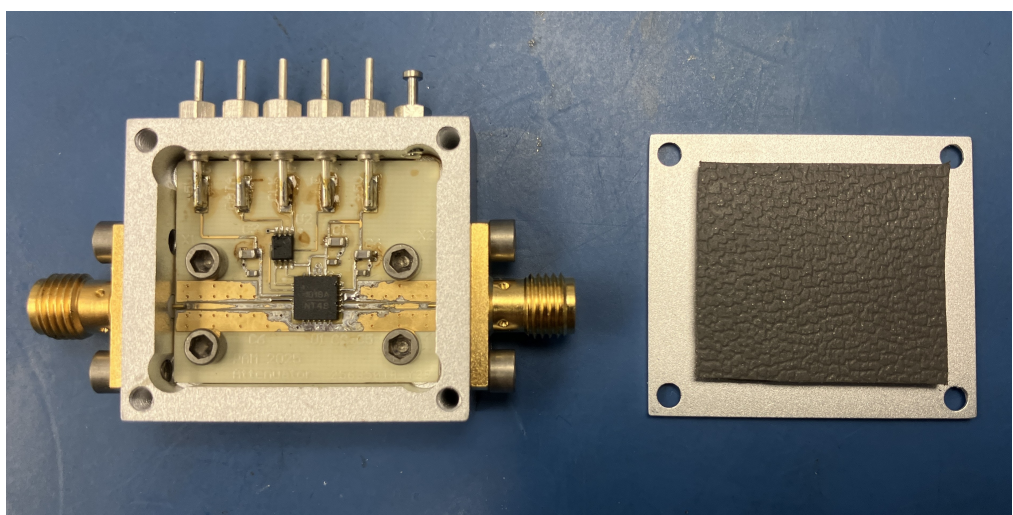


Figure 39: Assembled attenuator module inside the enclosure, with RF absorber material placed on the inside of the lid.

The measurement setup is identical to the one used for the previous prototype, which included multiple attenuators and amplifiers (see Figure 28). In Figure 40, the performance of the attenuator module is compared with a commercially available evaluation board for the same attenuator. Both were set to maximum attenuation.

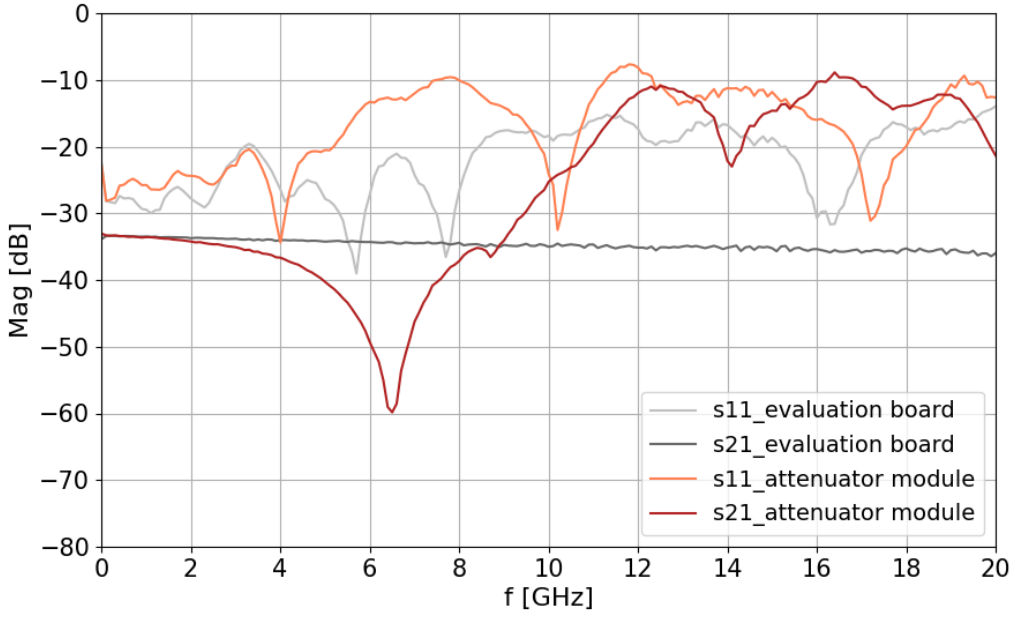


Figure 40: Measurement result of attenuator module (red) compared to attenuator evaluation board (gray).

The measurement results reveal that the attenuator module does not perform as expected. The S21 parameter exhibits significant variance, similar to the previous prototype that used the same attenuators alongside amplifiers (see Figure 29). This suggests that the issue originates either from the attenuator or its surrounding layout, rather than from radiation effects.

To identify the cause, a systematic exclusion approach was applied. Replacement of the attenuator had no effect, ruling out a faulty component. The evaluation board performed well, confirming that the attenuator model itself is not the root cause. In addition, even when the supply voltage was switched off for both the module and the evaluation board, the S21 trace of the module appeared significantly more irregular. This observation ruled out the power supply as a potential source of the issue. As the S11 parameter of the attenuator module remains predominantly below -10 dB, the SMA connectors are eliminated as primary sources of error. Furthermore, the amplifier and detector modules, which use the same CPW and SMA transitions, performed correctly. The trace-to-attenuator transitions are slightly different from those in the other two modules. However, HFSS simulations, consistent with the previous multi-attenuator prototype, suggest that they

should not significantly degrade performance (see Figure 27).

Based on these findings, the issue appears to stem from the footprint of the attenuator itself. To further investigate, the attenuator from the evaluation board was removed and its footprint compared to the one used in the attenuator module, as shown in Figure 41.

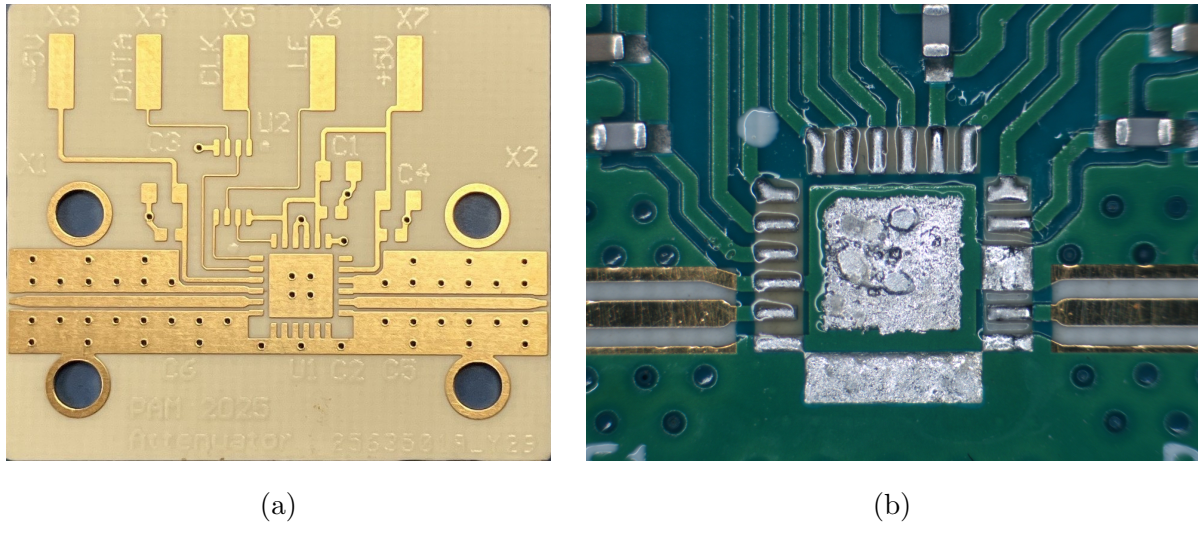


Figure 41: Comparison of the attenuator footprints: (a) attenuator module vs. (b) evaluation board.

Two significant differences were identified. Firstly, the ground plane in the attenuator module is narrowed over a longer distance to accommodate the input signal traces from above. Secondly, on the evaluation board, the ground pads next to the RF input and output are directly connected to the central ground pad. The second difference is likely the main cause of the performance degradation as it allows RF energy to escape from the trace rather than being properly guided. To address this issue, a revised prototype will be developed, with all ground pins connected to the central ground pad, preventing parts of the RF signal from escaping the trace. In addition, the routing of the upper input signals will be more direct, minimizing the narrowing of the ground plane.

Unlike the attenuator module, the amplifier and detector modules do not exhibit this issue. This becomes plausible when comparing their footprints, as shown in Figure 42.

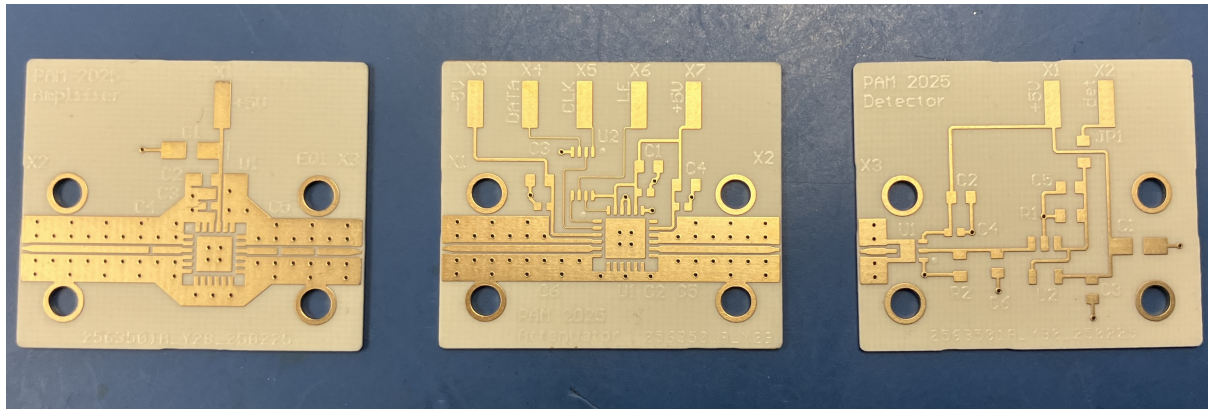


Figure 42: Comparison of module footprints: amplifier module (left), attenuator module (middle), and detector module (right).

The detector module has its ground pins connected to the central ground pad, while the amplifier module does not require as many input signals, avoiding ground-plane gaps where RF leakage could occur. Nonetheless, a new amplifier prototype will also be tested with connected ground pads around the RF input and output to determine whether further improvements can be made.

5.5 Detector Module

The design of the detector module is shown in Figure 44.

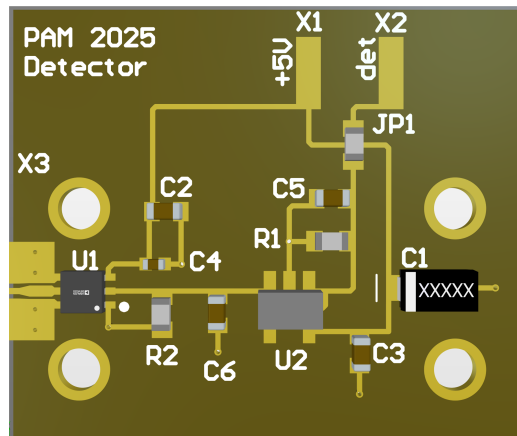


Figure 43: Prototype design of detector module.

The PCB includes a power detector (U1), along with multiple bypass capacitors and one kilo ohm resistors to ensure stable operation. One zero ohm resistor (JP1) allows the output signal to cross the supply voltage trace. In addition, an operational amplifier (U2) stabilizes the output voltage for reliable power detection. The wires for the +5 V supply

voltage and the output for power detection can be soldered on X1 and X2, respectively. X3 provides space for soldering the SMA connector for the RF input. As with the other modules, a ground wire can be directly connected to a pin in the conductive enclosure.

The assembly process followed the same reflow soldering procedure as described in Section 5.3. The fully assembled prototype is shown in Figure 44.

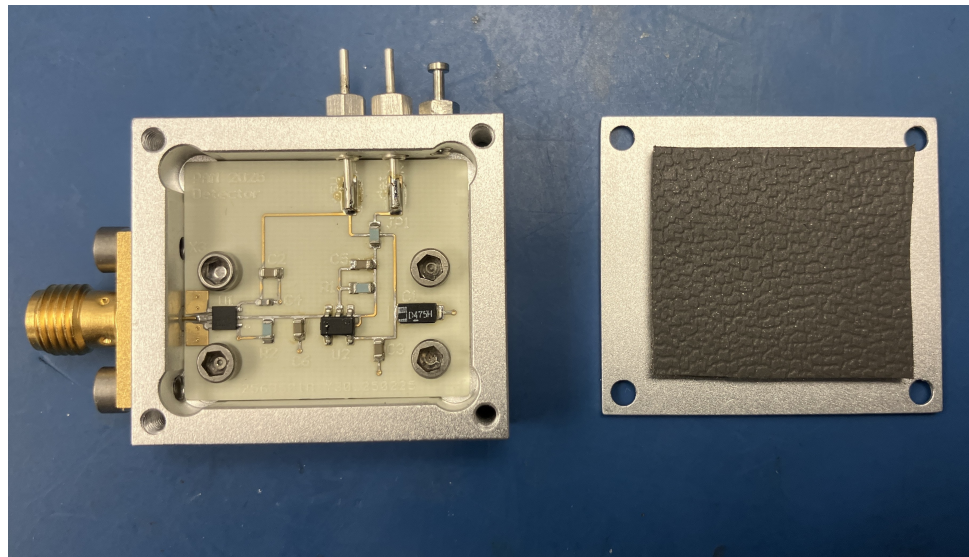


Figure 44: Assembled detector module inside the enclosure, with RF absorber material placed on the inside of the lid.

Since the detector module does not have an RF output, only the S11 parameter can be measured to assess signal reflection. The measurement setup is the same as in Figure 19, and the results are shown in Figure 45.

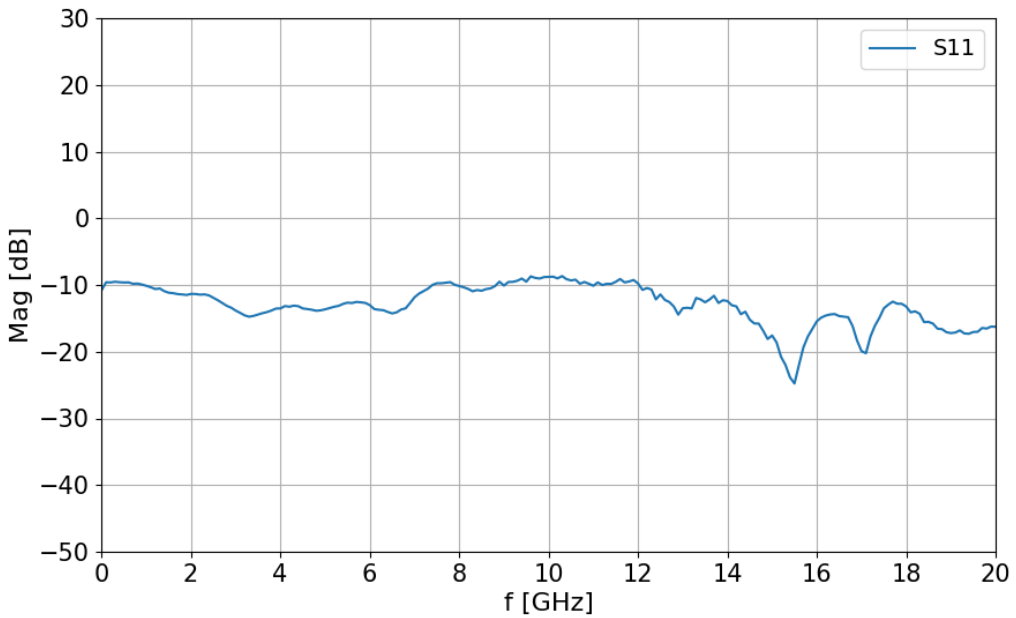


Figure 45: Measured S11 parameter of the detector module.

Overall, the S11 parameter of the detector module indicates rather good impedance matching. Only at about 8-12 GHz and below 1 GHz the S11 parameter slightly exceeds -10 dB.

The power detector diode converts the incoming RF signal power to a proportional output voltage. To correlate output voltage with input power levels, a second measurement was performed. The measurement setup is shown in Figure 46.

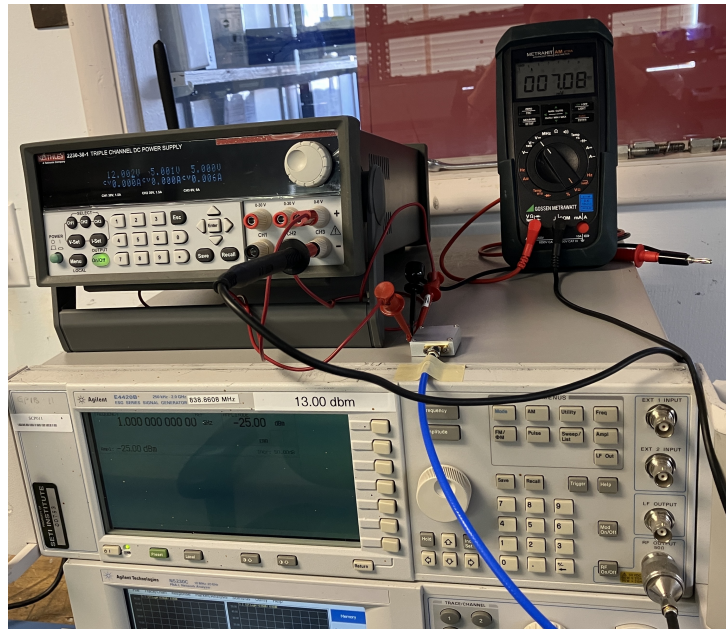
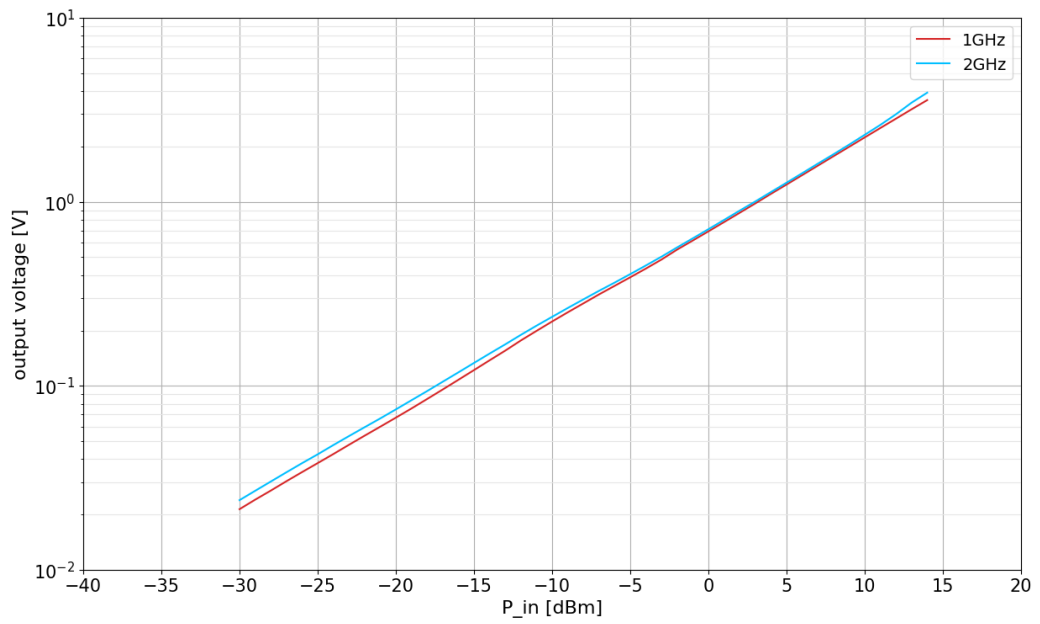


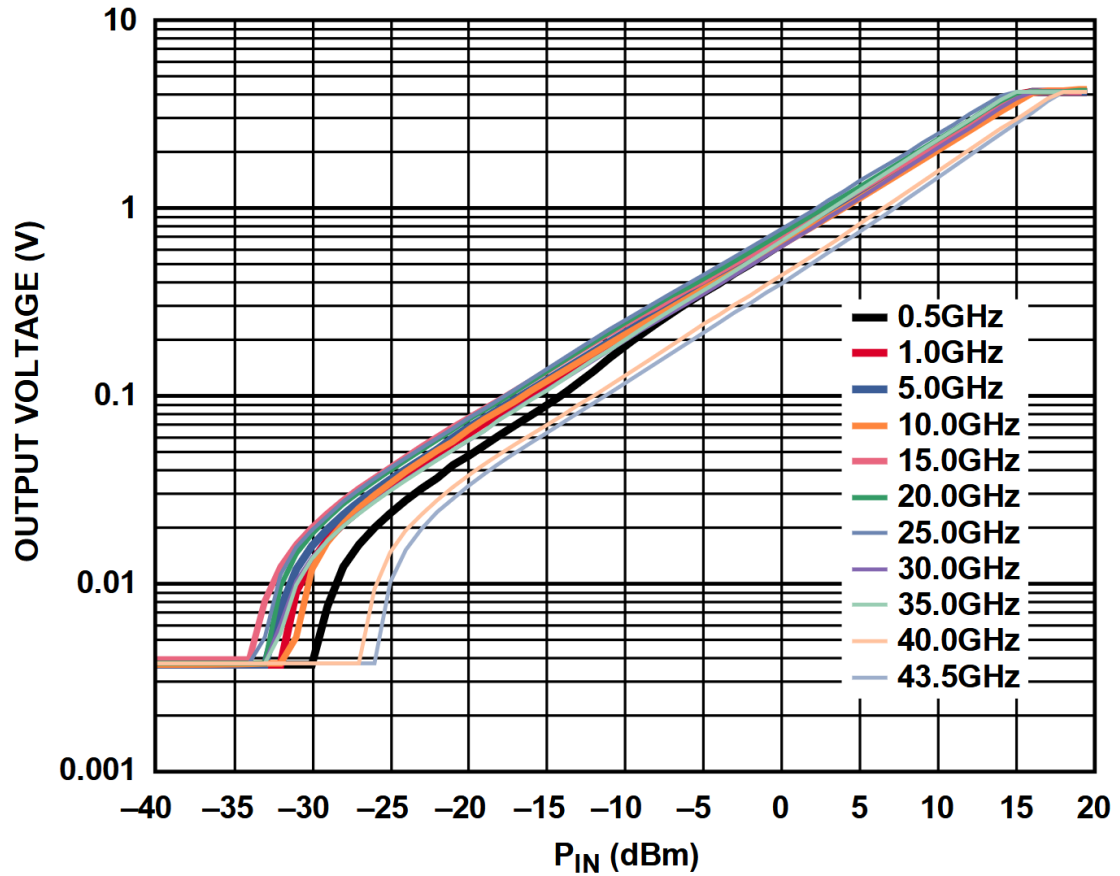
Figure 46: Measurement setup for power detection: prototype (center) connected to signal generator (bottom), power supply (left) and multimeter (right).

The signal generator (bottom) was used to apply an RF input with a fixed frequency and varying power levels. The power was increased stepwise and the corresponding output voltages were measured using a multimeter (upper right corner). The power supply (upper left corner) provided the required +5 V supply voltage to the detector module (center).

The resulting voltage-to-power curves for 1 GHz and 2 GHz are shown in Figure 47 and compared to the datasheet specifications of the ADL6010 power detector. The maximum frequency of the signal generator was 2 GHz.



(a) Measured voltage-to-power curve of detector module



(b) voltage-to-power curve from the ADL6010 power detector datasheet [10].

Figure 47: Comparison of voltage-to-power curves: (a) Measured detector module vs. (b) Datasheet reference.

The measured voltage-to-power curves of the detector module closely match the datasheet specifications of the ADL6010 power detector. This indicates that the power detection functionality is operating as expected, with accurate and reliable performance.

5.6 Summary

This chapter presented the modular design approach for the PAM. The three independent modules - amplifier, attenuator and detector module - were designed, assembled and tested separately. Simulation confirmed the successful optimization of the top ground plane size and the transitions to the SMA-connectors. The measurement results of the amplifier module indicate good performance. In contrast, the attenuator module relieved poor performance, traced to issues in the footprint design and ground plane layout. A revised prototype is planned to fix these problems. The S11-parameter of the detector module shows rather good impedance matching, while measurement of the voltage-to-power curve proved accurate and reliable power detection.

6 Conclusion

In this report, a phased approach was taken in developing the PAM for the ATA, starting with optimizing the signal trace and gradually integrating amplifiers, attenuators and other key components. The first prototype successfully minimized signal losses by implementing a coplanar waveguide. Subsequently, two amplifiers were tested and the MML098GQ4A amplifier was selected for its flat insertion loss curve and higher gain. Attempts to integrate multiple amplifiers and attenuators within the existing PAM enclosure were unsuccessful. Initially, the issues were attributed to excessive radiation within the enclosure, prompting the exploration of a modular design approach. However, further testing of subsequent prototypes revealed that the attenuator footprint was likely the primary cause of the problem.

Despite this, the modular design approach remains advantageous, as it reduces radiation and simplifies maintenance. The measurement of the amplifier and detector modules demonstrated promising performance, whereas the attenuator module exhibited poor results. A revised prototype for the attenuator module is planned, along with further refinements to the amplifier module. Once these improvements are implemented, the final design will be tested before full-scale production and integration into all antennas.

References

- [1] Sanders, R. (2007, October 11). *Radio telescope array dedicated to astronomy, SETI*. Retrieved February 24, 2025, from https://newsarchive.berkeley.edu/news/media/releases/2007/10/11_ata.shtml
- [2] Farah, W. (2023, November 06). *GNU Radio and the Allen Telescope Array*. Retrieved February 24, 2025, from https://casper.astro.berkeley.edu/workshop2023/agenda/presentations/day1/3_WF.pdf
- [3] Hat Creek Radio Observatory. (n. d.). *SETI at HCRO*. Retrieved March 01, 2025, from <https://github.com/SETIatHCRO/Front-Page>
- [4] Steer, M. (2024, January 01). *Co-Planar Waveguide*. Retrieved February 26, 2025, from [https://eng.libretexts.org/Bookshelves/Electrical_Engineering/Electronics/Microwave_and_RF_Design_II_-_Transmission_Lines_\(Steer\)/03%3A_Planar_Transmission_Lines/3.08%3A_Co-Planar_Waveguide](https://eng.libretexts.org/Bookshelves/Electrical_Engineering/Electronics/Microwave_and_RF_Design_II_-_Transmission_Lines_(Steer)/03%3A_Planar_Transmission_Lines/3.08%3A_Co-Planar_Waveguide)
- [5] Papió, A. (2009, January). *60 GHz material characterization and waveguide antenna array design*. Retrieved February 26, 2025 https://www.researchgate.net/publication/39680230_60GHz_material_characterization_and_waveguide_antenna_array_design
- [6] Pozar, D. M. (2011). *Microwave Engineering* (4th ed.). John Wiley & Sons.
- [7] Analog Devices. (n. d.). *HMC462LP5 / 462LP5E*. Retrieved March 05, 2025, from <https://www.analog.com/media/en/technical-documentation/data-sheets/hmc462.pdf>
- [8] Zheng G., Papapolymerou J., Tentzeris M. M. (2003, December 31). *Wideband coplanar waveguide RF probe pad to microstrip transitions without via holes*. Retrieved on March 05, 2025, from <https://ieeexplore.ieee.org/document/1261778>
- [9] Miller MMIC. (n. d.). *MML098GQ4A*. Retrieved March 05, 2025, from https://millermmic.com/pdf/mmic_amplifier/MML098GQ4A.pdf

[10] Analog Devices. (n. d.). *Datasheet ADL6010*. Retrieved March 26, 2025, from <https://www.analog.com/media/en/technical-documentation/data-sheets/adl6010.pdf>